Selective Inhibitor Detector of Ge-Doped Al-Mg Surface: Molecular Modeling Approach using DFT & TD-DFT Calculations

Fatemeh Mollaamin [1,*] 🆔 , **Sara Shahriari** [2] 🆔 , **Karim Zare** [3]

[1]   Department of Biology, Faculty of Science, Kastamonu University, Kastamonu, Turkey
[2]   Department of Chemistry, Central Tehran Branch, Islamic Azad University, Tehran, Iran
[3]   Department of Chemistry, Science and Research Branch, Islamic Azad University, Tehran, Iran
*   Correspondence: smollaamin@gmail.com (F.M.);

Abstract: The infrared spectra for each of these inhibitor-metal alloy surfaces have been introduced in the frequency range around 500 cm^{-1}-3500 cm^{-1} for benzotriazole→Al-Mg-Ge, 2-mercaptobenzothiazole → Al-Mg-Ge, and 8- hydroxyquinoline → Al-Mg-Ge; 500-4000 for 3-amino-1, 2, 4-triazole-5-thiol → Al-Mg-Ge with the sharpest peak approximately around 2000 cm-1, 3000 cm-1 for benzotriazole → Al-Mg-Ge, 2-mercaptobenzothiazole→Al-Mg-Ge, and 8- hydroxyquinoline → Al-Mg-Ge; 2000 cm-1, 4000 cm-1 for 3-amino-1, 2, 4-triazole-5-thiol → Al-Mg-Ge. Nuclear magnetic resonance has focused on the intra-atomic and interatomic interactions through a variety of high, medium, and low layers of the ONIOM method. Al-Ge(14), Al-Ge(19), and Al-Ge(21) in the Al-Mg-Ge alloy surface with the highest fluctuation in the shielding tensors of the NMR spectrum generated by intra-atomic interaction direct us to the most influence in the neighbor atoms generated by interatomic reactions of N→Al, O→ Al, S→ Al through the coating and adsorbing process of Langmuir adsorption.

Keywords: ONIOM; Langmuir adsorption; benzotriazole; 2-mercaptobenzothiazole; 8-hydroxyquinoline; 3-amino-1, 2, 4-triazole-5-thiol; Al-Mg-Ge; NMR; IR; UV-VIS; HOMO; LUMO.

1. Introduction

It has been observed that Al-Mg-Ge alloy represents the identical liquid progression to Al-Mg-Si alloy, and its equilibrium phase is β-Mg$_2$Ge based on its phase diagram. In some research, the liquid progression of Al-Mg-Ge alloys consisting of various particles of Mg$_2$Ge has been studied by TEM and HRTEM and hardness analysis to find the impact of Mg$_2$Ge particles on the age-hardening treatment of these alloys compounds [1].

Al-Mg-Ge alloys display the identical evolution of positron lifetime τ1C qualitatively with time as Al-Mg-Si alloys, as a primary reduction, pursued by a re-enhancement, after which τ1C falls to an equilibrium amount. But, for alloys with identical magnesium contents, germanium increases to remarkably slower aging kinetics than silicon because of the impacts of atomic binding energies. Increasing copper to Al-Mg-Ge and Al-Mg-Si alloys calms down the primary configuration of complexes but develops their further outcome [2].

The special alloying elements that form aluminum alloys are Cu, Mg, Mn, Si, Sn, Ni, and Zn. Aluminum alloys' lightweight or corrosion resistance makes them suitable for engineering structures and components [3].

Aluminum-silicon (Al-Si) is one of the most important aluminum alloys with high amounts of silicon in casting and has a large limitation of usages in the aerospace and automotive industries through the best combination of mechanical properties, as well as good wear resistivity and corrosion resistance [4-6]. Si element in Al-Si-based cast alloys impacts tensile properties at both room and high temperatures, but its role becomes more important in the lack of alloy elements such as Mg, Fe, and Cu [7]. Some elements like Cu and Mg added to Al alloys ameliorate the mechanical attributes and conduct the alloy to reply to the heat dealing. The existence of magnesium also increases resistance and reduces the rate of strength loss at high temperatures in the alloys. Aluminum-magnesium (Al-Mg) alloys are lighter than other aluminum alloys and much less flammable than other alloys consisting of high amounts of magnesium. The magnificent enhancement in resistance at elevated temperature was accomplished after solution treatment through activating settlement, becoming hard through Mg possessing phases. Aluminum-Gallium (Al-Ga), which is a degenerate alloy, is obtained from liquid gallium diffusing the crystal structure of Ga metal. This alloy is so fragile that it is broken under a little pressure. Al-Ga alloy is also chemically more fragile because it prevents Al from forming a protective oxide layer. This element and its alloys are usually employed as experimental fluids for modeling liquid and solid dynamics in planetary cores. Al-Ga is able to react with H_2O molecules to produce Al oxide, Ga metal, and hydrogen gas. Al reacts in air to generate an inactive aluminum oxide layer and doesn't react with water. Aluminum-Gallium alloy can form Al nanoparticles for the hydrogen-creating reaction [8].

Among the various methods that minimize metal surface corrosion, its inhibition by organic molecules is one of the most applicable methods because of its stability and low cost [9-13]. Therefore, much research has been dedicated to applying efficient heterocyclic and heteroatomic, including organic compounds that ameliorate the anticorrosion attributes of metal surfaces and alloys. The existence of heteroatoms containing O, S, N, and P atoms, aromatic rings, and multiple bonds with π-electrons in these inhibitors extensively help form inactive blocks on the metal surface and alloys, so closing the active sites of corrosion [14-20].

Based on some research, benzotriazole, 2-mercaptobenzothiazole, 8-hydroxyquinoline, and 3-amino-1, 2, 4-triazole-5-thiol are organic cyclic inhibitors for metal, semi-metals, or non-metals surfaces and their alloys by preventing undesirable surface reactions. It is obvious that a passive layer, containing a complex between the surface and these inhibitors, is generated when the surface is immersed in a solution consisting of benzotriazole, 2-mercaptobenzothiazole, 8- hydroxyquinoline, and 3-amino-1, 2, 4-triazole-5-thiol [21-23].

In the present work, we have investigated adding some magnesium and silicon alloying elements to the aluminum surface, forming an A-Mg-Si complex coated with benzotriazole organic compounds, 2-mercaptobenzothiazole, 8- hydroxyquinoline, and 3-amino-1, 2, 4-triazole-5-thiol as the corrosion inhibitors of Al-Mg-Ge alloy surface.

2. Materials and Methods

2.1. Organic corrosion inhibitors.

Some researchers have investigated that organic compounds can be employed as corrosion inhibitors for Al and its alloys because they consist of several heteroatoms (N, S, O,

and P) that act as active adsorption centers. In this verdict, we discuss the use of organic compounds of benzotriazole, 2-mercaptobenzothiazole, 8- hydroxyquinoline, and 3-amino-1, 2, 4-triazole-5-thiol as the corrosion inhibitors of Al-Mg-Ge alloy surface [24].

This research has attributed the inhibiting effect of the benzotriazole, 2-mercaptobenzothiazole, 8- hydroxyquinoline, and 3-amino-1, 2, 4-triazole-5-thiol on the adsorption of a stable complex formed on the aluminum alloy of Al-Mg-Ge surface.

2.2. Langmuir adsorption theory.

The verdict dealing with the influence of the organic inhibitors in solution and the nature of the corrosive aluminum alloys on the adsorption bond strength yield information about the mechanism of interaction of the inhibitor with the Al alloys surface, which in turn Langmuir adsorption isotherms provide excellently. The Langmuir isotherm is widely used in the identification of inhibitor adsorption status specification [25,26]

The adsorption of benzotriazole, 2-mercaptobenzothiazole, 8- hydroxyquinoline, and 3-amino-1, 2, 4-triazole-5-thiol as corrosion inhibitors on the aluminum alloy surface of Al-Mg-Ge in NaCl solution were assigned by the most suitable Langmuir isotherm, which exhibits the chemisorptive nature of the bond between the inhibitor molecules and the Al-Mg-Ge alloy surface, the equilibrium distribution of ions of the adsorbing compound between the solid and liquid phases, and a monolayer attribute.

The adsorbed molecules are kept on the Al-Mg-Ge alloy surface with highly protected chemisorbed inhibitors (Scheme 1).
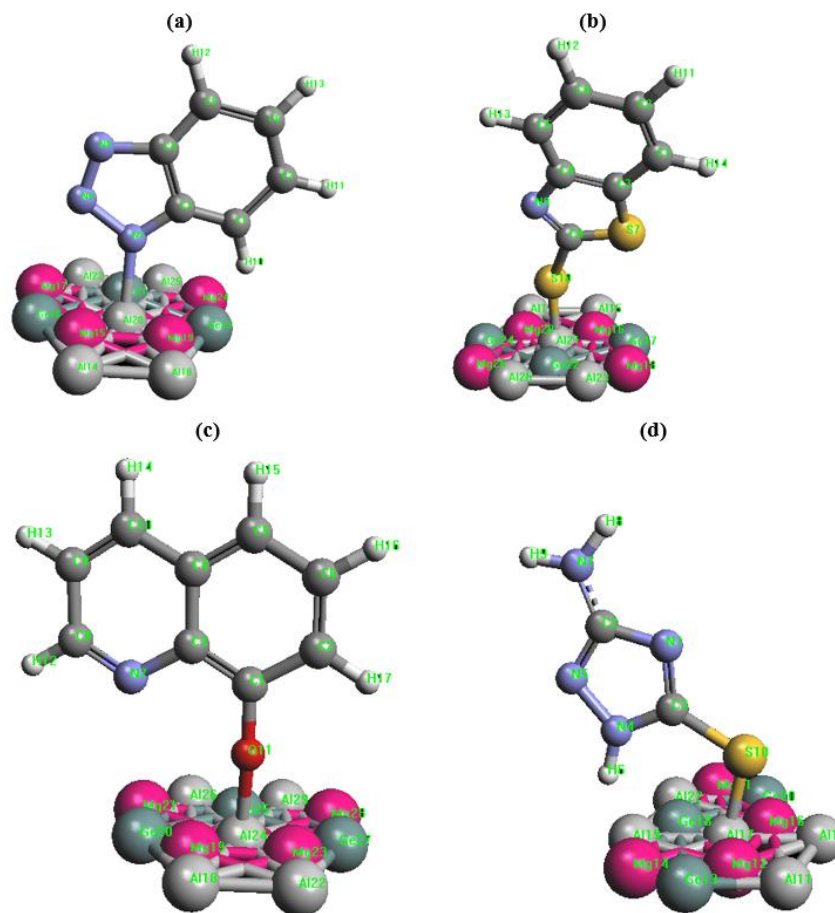
Scheme 1. Langmuir adsorption of the organic corrosion inhibitors of **(a)** benzotriazole; **(b)** 2-mercaptobenzothiazole; **(c)** 8- hydroxyquinoline; **(d)** 3-amino-1, 2, 4-triazole-5-thiol onto Al-Mg-Ge alloy surface.

2.3. ONIOM method.

This research defines the combination of three levels of the ONIOM method in decreasing order of accuracy, including high, medium, and low levels of theory. High-level has been done using the DFT method of Cam-B3LYP with 6-31+G(d,p) basis set for some hydrogen, carbon, oxygen, sulfur, and also some silicon atoms in the adsorption site, EPR-III basis set for nitrogen and LANL2DZ for some aluminum and magnesium atoms in the adsorption sites. Medium-level has been done on the adsorption sites' hydrogen, carbon, nitrogen, oxygen, and sulfur due to semi-empirical methods. Finally, a low-level has been performed on the other aluminum, magnesium, and silicon atoms with MM2 force fields (Scheme 2) [27]
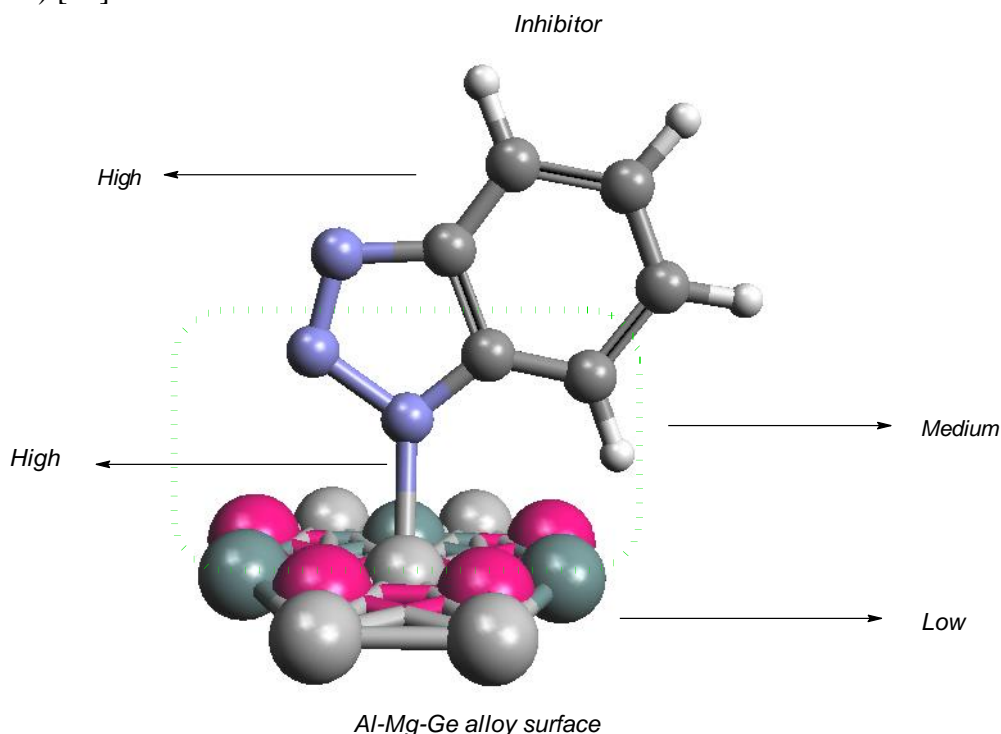
Scheme 2. The ONIOM layer of adsorption mechanism for 3-amino-1, 2, 4-triazole-5-thiol as a corrosion inhibitor onto Al-Mg-Ge alloy surface based on optimized coordination.

On the other hand, the three-layered method of ONIOM lets us discover a larger system more exactly than the one-layered model, which could behave as a medium size system precisely like a ground system with acceptable accuracy [28].

Therefore, this three-layered pattern has been applied for effective barriers of benzotriazole, 2-mercaptobenzothiazole, 8- hydroxyquinoline, and 3-amino-1, 2, 4-triazole-5-thiol adsorbing onto Al-Mg-Ge alloy surface (Scheme2).

We have calculated the structures using the density functional theory (DFT) on the mechanisms onto Al-Mg-Ge alloy surfaces up to adsorbed in the active sites of organic inhibitors by nitrogen, oxygen, and sulfur atoms of benzotriazole, 8- hydroxyquinoline, 2-mercaptobenzothiazole, and 3-amino-1, 2, 4-triazole-5-thiol, respectively.

We have found that the surface binding site preferences of N-atom of benzotriazole, O-atom of 8- hydroxyquinoline and S-atom of 2-mercaptobenzothiazole and 3-amino-1, 2, 4-triazole-5-thiol in adsorption site is largely affected by the presence of neighboring atoms. The calculated N→Al, O→Al, and S→Al pair distribution functions have indicated that the formation of clusters directs to shorter N→Al, O→Al, and S→Al bond lengths when compared to the homogeneous growth (Scheme 2).

In this work, the atomic structure of the Al-Mg-Ge alloy surface has been built using GaussView 6.06.16 [29] and calculated by Gaussian 16 program package [30] through geometry coordination. Result observations have represented that the Al-Mg-Ge alloy surface calculated with the achieved structure parameters is in good agreement with those metal alloys attained from other experimental calculations [31-36].

2.4. DFT calculations.

Hybrid functional is a group of approximations for the exchange-correlation energy functional in DFT (Density Functional Theory), which combines a part of exact exchange from HF (Hartree–Fock theory) method with the rest of the exchange-correlation energy from other information such as empirical or ab initio methodologies [37-43].

Therefore, the Kohn- Sham orbitals illustrate the exact exchange energy functional instead of the density, which is placed as the indirect density functional. This study has applied the influence of the hybrid functional of the three-parameter basis set of B3LYP (Becke, Lee, Yang, Parr) within the framework of DFT upon theoretical calculations [44-49].

The Al-Mg-Ge alloy surface has been built by a rigid system and Z-Matrix format in which a blank line has been placed, and after that, the following information has been illustrated. The rigid PES has been performed at CAM-B3LYP functional [50], and employing 6-31+ G (d,p) /EPRIII /LANL2DZ basis sets to assign HOMO, LUMO, Mulliken charges, nuclear magnetic resonance properties, dipole moment, thermodynamic characteristics and other quantum properties for this study [51] for benzotriazole, 8- hydroxyquinoline, 2-mercaptobenzothiazole, and 3-amino-1, 2, 4-triazole-5-thiol adsorbing onto the Al-Mg-Ge alloy surface using Gaussian 16 program package [30]. The input files for the organic corrosion inhibitors adsorbed onto the Al-Mg-Ge surface have been provided with GaussView 6.06.16 [29].

3. Results and Discussion

Most inhibitors deduce or prohibit aluminum corrosion by either cathode or anodic reactions [52,53]. The usage of chromates (which extinguish the anodic reactions with coatings as the inhibitions for aluminum sheets) has reduced because of toxicity. Other compounds like phosphates, silicates, nitrates, nitrites, benzoates, and N-heterocyclic structures can influence the cathodic reactions in an aqueous environment.

In this article, the susceptibility of organic inhibitors (benzotriazole, 2-mercaptobenzothiazole, 8- hydroxyquinoline, and 3-amino-1, 2, 4-triazole-5-thiol), characteristics of aluminum alloy surface (Al-Mg-Ge) and adsorption conditions are considerable.

3.1. Infrared spectroscopy analysis.

The IR spectrum for each of these compounds has been seen in the frequency range around 500 cm^{-1}-3500 cm^{-1} for benzotriazole→Al-Mg-Ge, 2-mercaptobenzothiazole→Al-Mg-Ge, and 8- hydroxyquinoline→Al-Mg-Ge; 500-4000 for 3-amino-1, 2, 4-triazole-5-thiol →Al-Mg-Ge with the sharpest peak approximately around 2000 cm^{-1}, 3000 cm^{-1} for benzotriazole→Al-Mg-Ge, 2-mercaptobenzothiazole→Al-Mg-Ge, and 8-hydroxyquinoline→Al-Mg-Ge; 2000 cm^{-1}, 4000 cm^{-1} for 3-amino-1, 2, 4-triazole-5-thiol→Al-Mg-Ge (Figure1a-d).
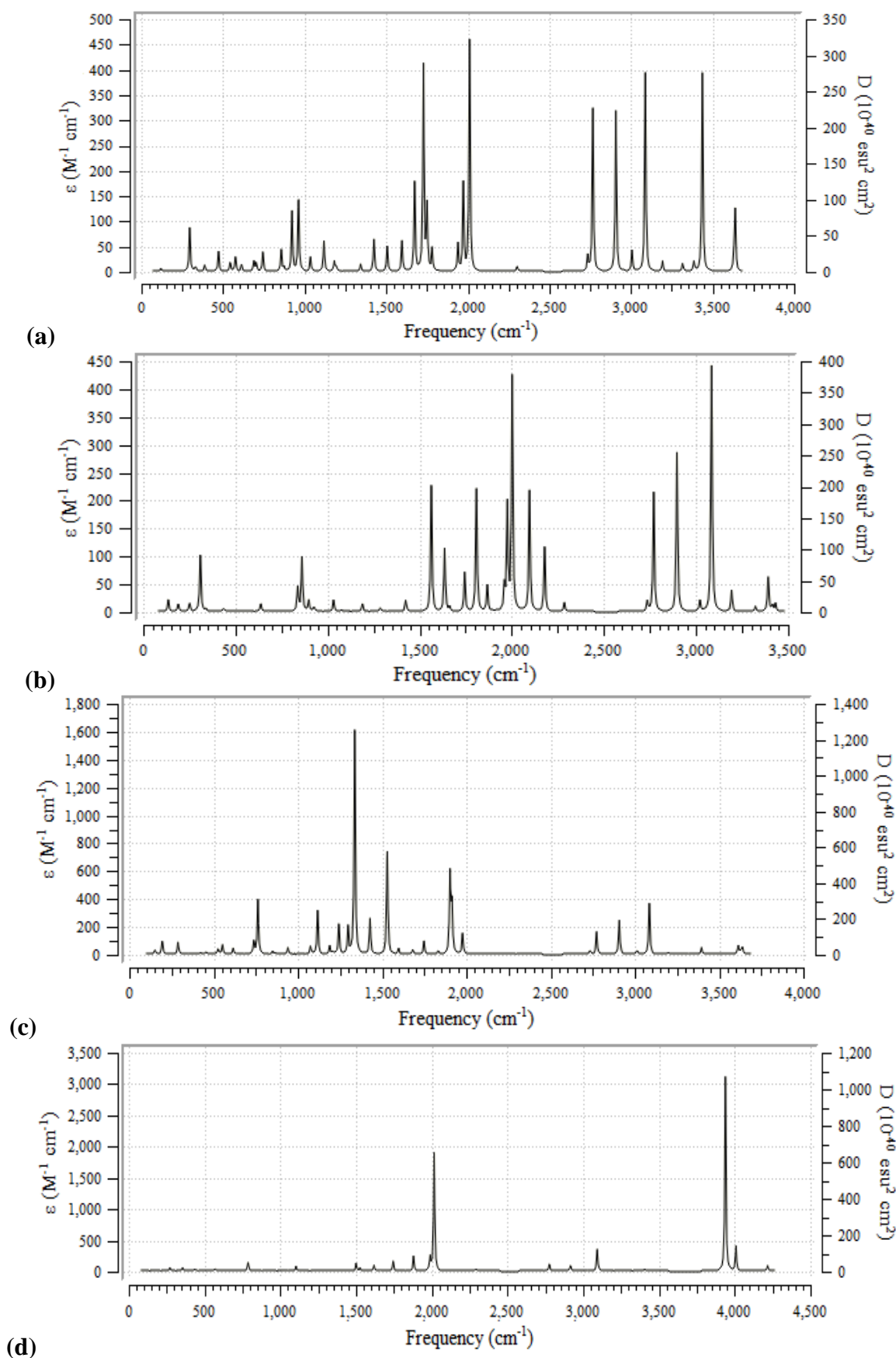
Figure 1. Changes of frequency (cm^{-1}) through the IR spectra for **(a)** benzotriazole → Al-Mg-Ge, **(b)** 2-mercaptobenzothiazole→ Al-Mg-Ge, **(c)** 8- hydroxyquinoline → Al-Mg-Ge, and **(d)** 3-amino-1, 2, 4-triazole-5-thiol → Al-Mg-Ge using CAM-B3LYP method with 6-31+ G (d,p) /EPRIII /LANL2DZ basis sets.

The infrared (IR) calculations have been accomplished for the aluminum alloy of Al-Mg-Ge interacting with four organic inhibitors, including benzotriazole, 2-mercaptobenzothiazole, 8- hydroxyquinoline, and 3-amino-1, 2, 4-triazole-5-thiol adsorbed onto this alloy surface which produces the complexes of benzotriazole → Al-Mg-Ge, 2-mercaptobenzothiazole→ Al-Mg-Ge, 8- hydroxyquinoline → Al-Mg-Ge, and 3-amino-1, 2, 4-triazole-5-thiol → Al-Mg-Ge at CAM-B3LYP level of theory employing 6-31+ G (d,p) /EPRIII /LANL2DZ basis sets to obtain the more accurate equilibrium geometrical parameters, physical and thermodynamic properties for each of the determined structure (Table 1).

Table 1. The Physico-chemical properties of adsorption for benzotriazole, 2-mercaptobenzothiazole, 8-hydroxyquinoline, and 3-amino-1, 2, 4-triazole-5-thiol as corrosion inhibitors on the aluminum alloy surface of Al-Mg-Ge in NaCl solution at 300K.

Compound	$\Delta H^o \times 10^{-4}$ (kcal/mol)	$\Delta G^o \times 10^{-4}$ (kcal/mol)	S^o (cal/K.mol)	Dipole moment (Debye)
Al-Mg-Ge	-512.9295	-512.9319	79.090	1.5308
Benzotriazole	-24.5172	-24.5196	80.255	3.3166
Benzotriazole → Al-Mg-Ge	-534.6511	-534.6539	91.304	4.8665
2-mercaptobenzothiazole	-69.5234	-69.5260	85.643	2.5108
2-mercaptobenzothiazole→ Al-Mg-Ge	-579.6409	-579.6437	94.592	3.1465
8- hydroxyquinoline	-29.5526	-29.5551	83.336	1.6389
8- hydroxyquinoline → Al-Mg-Ge	-539.6983	-539.7011	94.441	2.1269
3-amino-1, 2, 4-triazole-5-thiol	-43.1336	-43.1358	73.839	1.5672
3-amino-1, 2, 4-triazole-5-thiol → Al-Mg-Ge	-553.2600	-553.2627	90.820	2.2141

From Figure 2, it could be found that the maximum of the Langmuir adsorption isotherm plots based on ΔG^o_{ads} may depend on the interactions between the inhibitor structures and the Al-alloy surfaces. In fact, in comparison to ΔG^o_{ads} amounts confirmed a good agreement among calculated results, as well as the correctness of the selected isotherm for the adsorption process of benzotriazole → Al-Mg-Ge, 2-mercaptobenzothiazole→ Al-Mg-Ge, 8-hydroxyquinoline → Al-Mg-Ge, and 3-amino-1, 2, 4-triazole-5-thiol → Al-Mg-Ge (Figure 2).
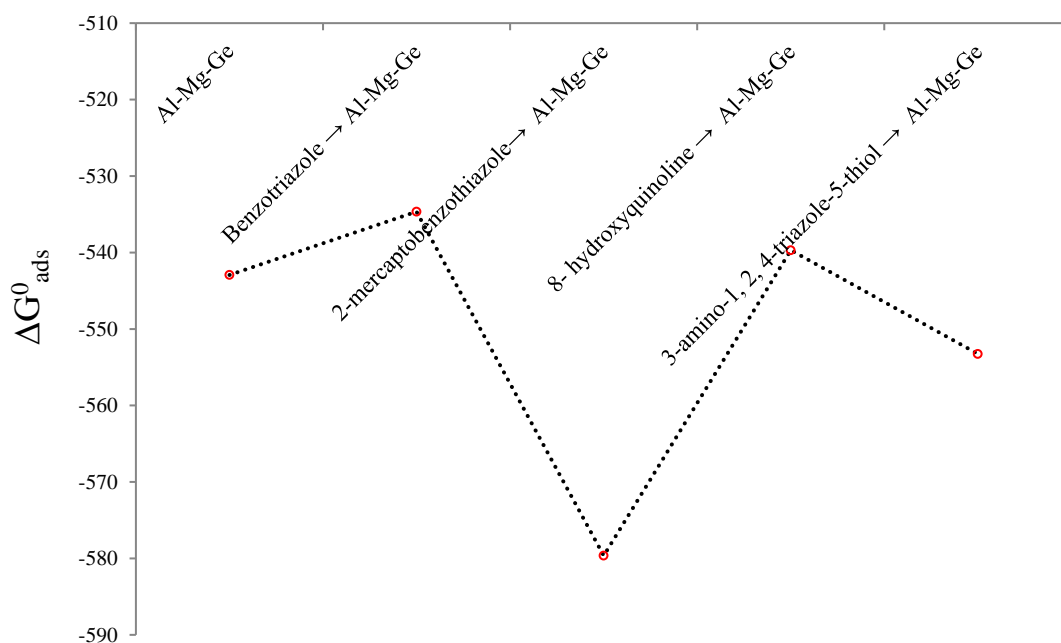
Figure 2. The changes of Gibbs free energy for adsorption of benzotriazole, 2-mercaptobenzothiazole, 8-hydroxyquinoline, and 3-amino-1, 2, 4-triazole-5-thiol as corrosion inhibitors on the Al-Mg-Ge alloy surface in NaCl solution at 300K.

The adsorptive capacity of inhibitor structures on the Al-Mg-Ge alloy surface is approved by the ΔG_{ads}^o amounts:

$$\Delta G_{ads}^o = \Delta G_{inh \to [Al-Mg-Ge]}^o - \left(\Delta G_{inh}^o + \Delta G_{[Al-Mg-Ge]}^o \right) \qquad (1)$$

On the basis of the data in Table 1, it is predicted that the adsorption of the inhibitor on the Al-Mg-Ge alloy surface might be physical and chemical. As shown in Figure2, all the computed ΔG_{ads}^o amounts are very close, which exhibits the agreement of the evaluated data by all methods and the validity of the computations, and it has also represented the maximum fluctuation for benzotriazole → Al-Mg-Ge, 2-mercaptobenzothiazole → Al-Mg-Ge, 8-hydroxyquinoline → Al-Mg-Ge, and 3-amino-1, 2, 4-triazole-5-thiol → Al-Mg-Ge, respectively (Figure2). Moreover, 2-mercaptobenzothiazole → Al-Mg-Ge has shown the sharpest peak in ΔG_{ads}^o amount which displays the most stability in the coating process of the Al-Mg-Ge alloy surface with 2-mercaptobenzothiazole.

3.2. NMR analysis.

The heterocyclic organic inhibitors of benzotriazole, 2-mercaptobenzothiazole, 8-hydroxyquinoline, and 3-amino-1, 2, 4-triazole-5-thiol have approximately shown identical behavior (20-2000 ppm) for various atoms in the active sites of these compounds through the NMR properties (Figure3a-d). The sharpest peak of the NMR spectrum has been almost observed between 20 ppm for these compounds. The weakest peaks of the NMR spectrum have approximately appeared in 400ppm-1000ppm for all four heterocyclic organic inhibitors containing benzotriazole, 2-mercaptobenzothiazole, 8- hydroxyquinoline, and 3-amino-1, 2, 4-triazole-5-thiol adsorbed on the Al-Mg-Ge alloy surface (Figure3a-d).

(a)

(b)

(c)

(d)
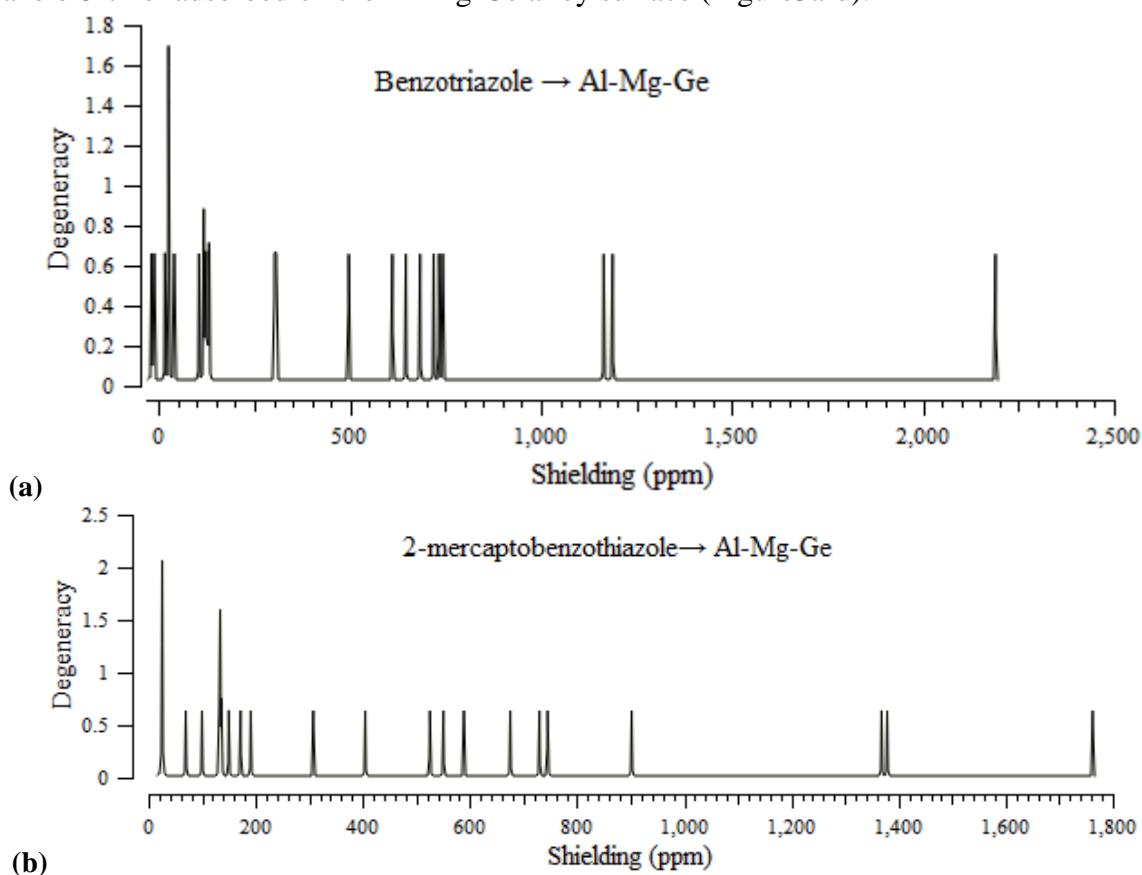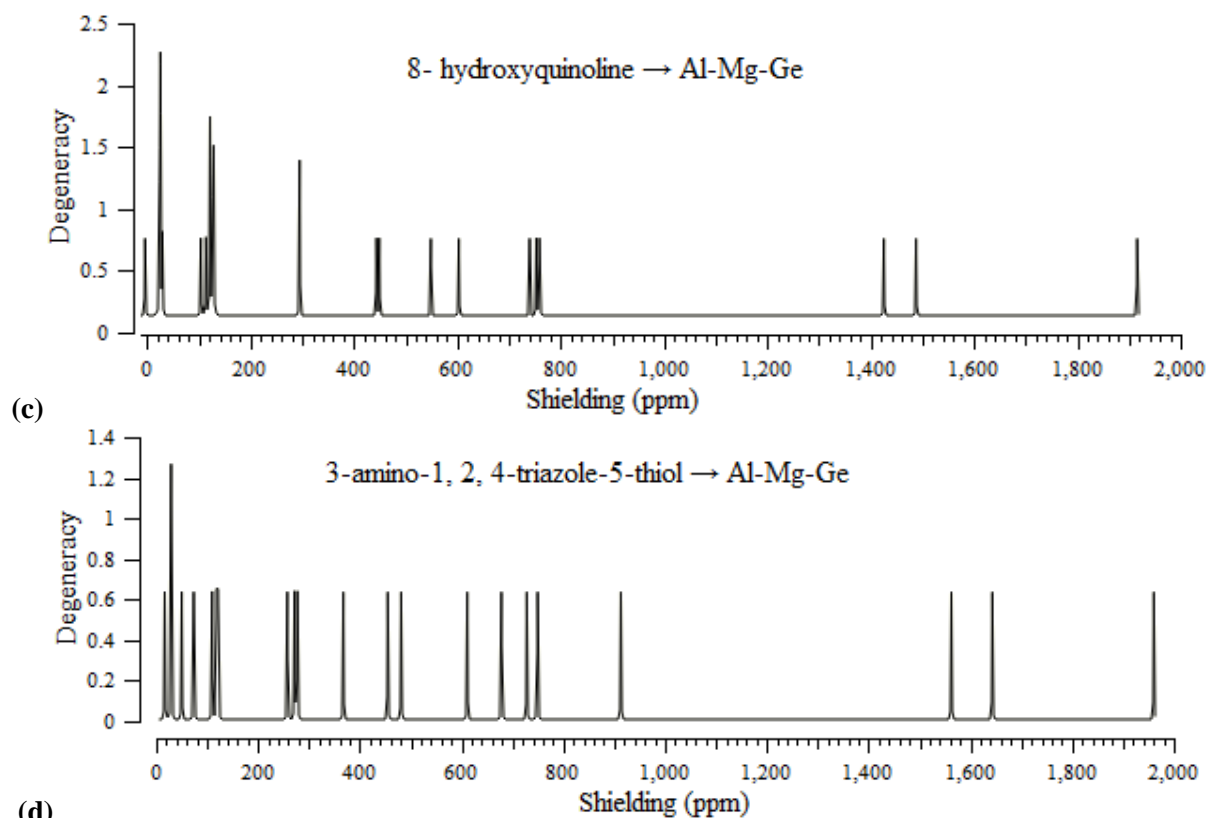
Figure 3. Chemical shift of NMR spectroscopy for **(a)** benzotriazole → Al-Mg-Ge, **(b)** 2-mercaptobenzothiazole → Al-Mg-Ge, **(c)** 8- hydroxyquinoline → Al-Mg-Ge, and **(d)** 3-amino-1, 2, 4-triazole-5-thiol → Al-Mg-Ge; through the Langmuir adsorption process by indicating the active nitrogen, oxygen, and sulfur atoms in heterocyclic compounds becoming close to the nanosurface.

Then, the atomic charge and NMR data of isotropic (σ_{iso}) and anisotropic shielding tensor (σ_{aniso}) for benzotriazole → Al-Mg-Ge, 2-mercaptobenzothiazole→ Al-Mg-Ge, 8-hydroxyquinoline → Al-Mg-Ge, and 3-amino-1, 2, 4-triazole-5-thiol → Al-Mg-Ge have been calculated using Gaussian 16 revision C.01 software [30] and reported in Tables 2.

The quantum chemical calculations yield the CS tensors in the principal axes system to evaluate the isotropic chemical shielding (CSI) and anisotropic chemical shielding (CSA) [54]:

$$CSI \text{ (ppm)} = (\sigma_{33} + \sigma_{22} + \sigma_{11})/3 \qquad (2)$$
$$CSA \text{ (ppm)} = \sigma_{33} - (\sigma_{22} + \sigma_{11})/2 \qquad (3)$$

The nuclear magnetic resonance (NMR) calculation for chemical shifts for assigning the structural and geometrical of compounds has been accomplished [55-63].

In fact, Gauge Invariant Atomic Orbital (GIAO) method has been suggested as an accurate method for NMR parameter calculations, and ONIOM has obtained much attention for achieving NMR chemical shifts in inhibitor-surface complexes, for instance, isotropic chemical shielding becomes:

$$\sigma_{iso,ONIOM} = \sigma_{iso,high(QM1)} + \sigma_{iso,medium(QM2)} + \sigma_{iso,low(QM3)} \qquad (4)$$

Table 2. Atomic charge and NMR properties of some atoms of benzotriazole, 2-mercaptobenzothiazole, 8-hydroxyquinoline, and 3-amino-1, 2, 4-triazole-5-thiol in ppm adsorbed onto Al-Mg-Ge alloys surface.

Benzotriazole → Al-Mg-Ge				2-mercaptobenzothiazole→ Al-Mg-Ge			
Atom number	σ CSI	σ CSA	Q	Atom number	σ CSI	σ CSA	Q
C1	117.9760	130.9962	-0.0447	C1	136.0024	122.7119	0.0007

Benzotriazole → Al-Mg-Ge				2-mercaptobenzothiazole→ Al-Mg-Ge			
Atom number	σ CSI	σ CSA	Q	Atom number	σ CSI	σ CSA	Q
C2	117.2848	148.4955	-0.0084	C2	133.5741	132.9473	-0.0089
C3	131.9856	134.0405	0.0199	C3	149.8577	98.9333	-0.2353
C4	105.0113	55.3009	0.0437	C4	133.7886	90.2259	0.0727
C5	130.3074	128.2727	0.0097	C5	134.2643	130.3512	0.0125
C6	123.3779	127.3046	-0.0168	C6	132.2022	133.2009	-0.0085
N7	-18.9173	161.5640	-0.2648	S7	675.2650	262.5710	0.4940
N8	-12.1614	136.2061	-0.0838	C8	99.8362	83.2191	-0.2103
N9	40.2834	309.4109	-0.1594	N9	69.6504	348.2030	-0.282
Al10	611.2560	568.1077	0.1235	S10	171.8571	590.1696	0.1092
Mg11	733.4757	285.9863	-0.0339	Al11	404.5365	1291.3189	0.1022
Ge12	1164.3754	1920.7767	0.3814	Mg12	744.9366	404.0383	0.0335
Mg13	307.5064	526.5058	0.1836	Ge13	1378.8148	1358.3017	0.2842
Al14	683.7863	509.7169	0.1441	Mg14	307.6290	524.9416	0.1241
Mg15	743.0914	281.9001	-0.0183	Al15	525.2531	578.6307	0.1439
Al16	719.2745	631.6899	-0.6191	Mg16	729.6987	364.5323	-0.0316
Ge17	2189.9083	2513.6616	0.2163	Al17	901.9038	547.8662	-0.9123
Al18	496.9305	1642.2304	-0.1654	Ge18	1762.5073	1796.5923	0.1345
Ge19	1187.5821	2180.3583	0.2969	Al19	588.7922	748.0883	-0.1441
Mg20	302.8329	814.1690	0.1473	Ge20	1368.3920	1405.7363	0.3054
Al21	646.5255	953.7560	-0.1516	Mg21	190.8978	684.0134	0.1407
				Al22	550.5074	877.3522	-0.1243

8- hydroxyquinoline → Al-Mg-Ge				3-amino-1, 2, 4-triazole-5-thiol → Al-Mg-Ge			
Atom number	σ CSI	σ CSA	Q	Atom number	σ CSI	σ CSA	Q
C1	103.6673	98.3046	0.0908	N1	73.6610	227.4625	-0.3012
C2	128.5920	125.5311	-0.0253	C2	109.9727	96.5640	0.2190
C3	120.9835	121.1321	0.0382	C3	118.3564	94.0803	0.0056
C4	126.8268	157.4817	-0.0095	N4	121.5798	152.1964	-0.0131
C5	128.3212	120.9892	-0.0252	N5	50.1427	164.7410	-0.2188
C6	121.4315	140.6711	-0.0005	N6	277.5243	34.0255	0.0498
N7	-4.4329	514.3941	-0.2412	S7	367.6973	406.5485	0.2338
C8	113.4016	119.9238	0.0867	Al8	454.9255	940.1309	0.0936
C9	127.5471	138.2902	-0.0111	Mg9	728.2436	281.1538	-0.0192
C10	121.5269	130.3388	0.0042	Ge10	1643.3171	989.0809	0.3060
O11	29.2016	142.8936	-0.3004	Mg11	257.7681	549.0631	0.1104
Al12	443.5277	944.1353	0.1160	Al12	481.2472	1033.3120	0.0980
Mg13	758.9397	355.4279	-0.0509	Mg13	749.5681	169.9393	-0.1002
Ge14	1425.7826	1385.0785	0.3540	Al14	913.2231	388.2165	-0.7818
Mg15	294.8198	625.4089	0.1441	Ge15	1960.6673	1454.3191	0.0349
Al16	449.1545	912.8111	0.1082	Al16	678.5337	1012.6778	-0.1068
Mg17	752.9114	382.0734	-0.0227	Ge17	1562.7694	963.4386	0.3181
Al18	740.1272	642.3234	-0.5181	Mg18	271.7657	541.3623	0.14967
Ge19	1916.1387	1722.8962	0.1884	Al19	611.3117	1077.8319	-0.0779
Al20	548.8648	1054.3190	-0.1603				
Ge21	1488.1620	1260.0911	0.2828				
Mg22	294.8428	593.2067	0.1174				
Al23	603.0424	953.2960	-0.1656				

Besides, the solution of NaCl solution has influenced the nuclear magnetic resonance data and chemical shielding of carbon, nitrogen, oxygen, sulfur, aluminum, magnesium, and silicon in benzotriazole → Al-Mg-Ge, 2-mercaptobenzothiazole→ Al-Mg-Ge, 8-hydroxyquinoline → Al-Mg-Ge, and 3-amino-1, 2, 4-triazole-5-thiol → Al-Mg-Ge. In Figure 4, it has been indicated the chemical shielding tensors of isotropic (σ_{CSI}) and anisotropic (σ_{CSA}) of some effective atoms in the adsorption site of benzotriazole → Al-Mg-Ge, 2-

mercaptobenzothiazole → Al-Mg-Ge, 8- hydroxyquinoline → Al-Mg-Ge, and 3-amino-1, 2, 4-triazole-5-thiol → Al-Mg-Ge (Table 2). Figure 4 has certainly focused on the aluminum shielding in the intra-atomic interaction with magnesium and silicon and simultaneously interatomic interaction with other atoms in organic inhibitors through various high, medium, and low layers of the ONIOM method.
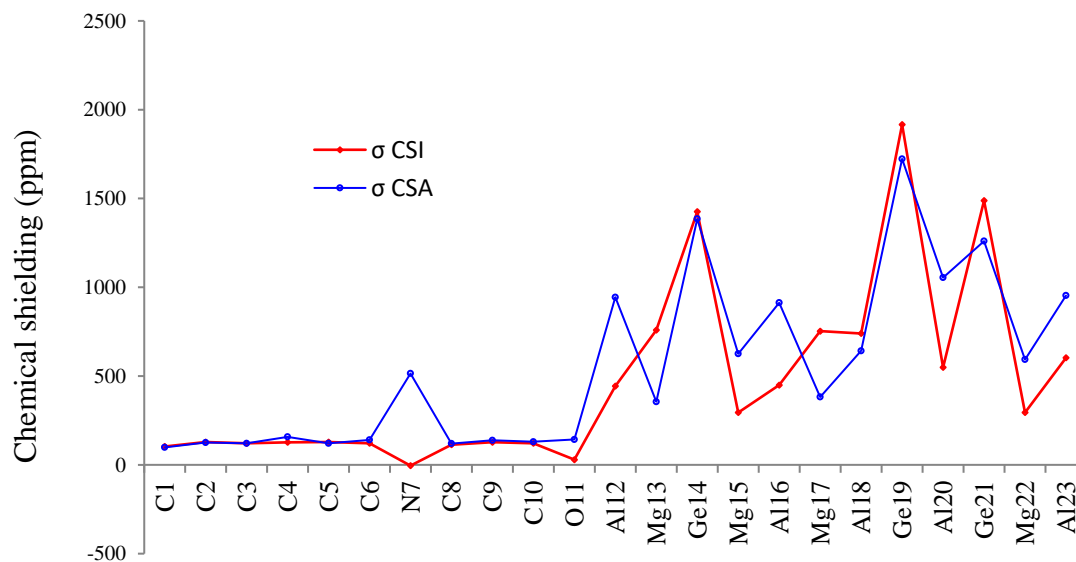
Figure4. The NMR plot of isotropic (σ_{iso}) and anisotropic (σ_{aniso}) shielding tensors for aluminum through intra-atomic interaction with magnesium and silicon atoms in alloy surface of Al-Mg-Ge and interatomic interaction with organic inhibitors in the adsorption site of (N→ Al, O→Al, S→Al) calculated by the level of theory CAM-B3LYP/6-31+G(d,p)/EPR-III/LANL2DZ.

Interatomic interactions, which is a related position of one, two, three, etc. atoms at a time, is written as a series expansion of functional parameters with interatomic potential [64]:

$$V = \sum_{i=1}^{N} V_1\left(\vec{r_i}\right) + \sum_{i,j=1}^{N} V_2\left(\vec{r_i},\vec{r_j}\right) + \sum_{i,j,k=1}^{N} V_3\left(\vec{r_i},\vec{r_j},\vec{r_k}\right) + \cdots \quad (5)$$

where V_1 is the one-body term, V_2 the two-body term, V_3 the three-body term, N the number of atoms in the system, $\vec{r_i}$ the position of atom i, $\vec{r_j}$ the position of atom j, the position of atom k, and i, j, k are indices that sprain around atom positions. In Figure 4, we have presented that the isotropic and anisotropy shielding increase with the occupancy and consequently, the negative charge of nitrogen, oxygen, and sulfur atoms in benzotriazole, 2-mercaptobenzothiazole, 8- hydroxyquinoline, and 3-amino-1, 2, 4-triazole-5-thiol diffusing onto Al-Mg-Ge alloy surface. It has been exhibited that the graph of nitrogen, oxygen, and sulfur atoms has the same attitude but a considerable deviation from carbon and hydrogen atoms. Intra-atomic interactions consist of Al-Al, Al-Mg, Al-Ge, Mg-Mg, Mg-Ge, Ge-Ge, and interatomic interactions are N → Al-Mg-Ge, O → Al-Mg-Ge, S→ Al-Mg-Ge based on the of CAM-B3LYP/6-31+G(d,p)/EPR-III/LANL2DZ quantum mechanics calculations using Gaussian 16 revision C.01 program (Figure 4). Based on Figure 4, it has been observed that Al-Ge(14), Al-Ge(19), and Al-Ge(21) direct us to the most influence in the neighbor atoms generated by interatomic reactions of N→Al, O→ Al, S→ Al in the Al-Mg-Ge alloy surface.

3.3. Nuclear quadrupole resonance (NQR).

Nuclear quadrupole resonance (NQR) frequency for benzotriazole → Al-Mg-Ge, 2-mercaptobenzothiazole→ Al-Mg-Ge, 8- hydroxyquinoline → Al-Mg-Ge, and 3-amino-1, 2, 4-triazole-5-thiol Al-Mg-Ge is proportional to the product of the nuclear quadrupole moment, a property of the nucleus, and the EFG in the neighborhood of the nucleus. As the EFG at the position of the nucleus in organic inhibitors is assigned by the valence electrons twisted in the special linkage with close nuclei of aluminum surface, the NQR frequency at which transitions happen is particular for an inhibitor → metal alloy complex (Table 2). In NMR, nuclei with spin≥ 1/2 have a magnetic dipole moment so that their energies are split by a magnetic field, permitting resonance sorption of energy dependent on the Larmor frequency; $\omega_L = \gamma B$, where γ is the gyromagnetic ratio, and B is the magnetic field external to the nucleus.

In NQR nuclei with spin≥ 1, there is an electric quadrupole moment which is accompanied by non-spherical nuclear charge distributions. So, the nuclear charge distribution deviates from that of a sphere as the oblate or prolate form of the nucleus [65,66].

NQR is a straight frame of the interaction of the quadrupole moment with the local electric field gradient (EFG), produced by its ambiance's electronic structure. Therefore, the NQR transition frequencies are symmetric to the electric quadrupole moment of the nucleus and a measure of the strength of the local EFG: $\omega \sim \frac{e^2\,Qq}{\hbar} = C_q$, where q is dependent on the biggest fundamental portion of the EFG tensor at the nucleus, and C_q is quadrupole coupling constant parameter [65,66]. The NQR method is based on the multipole expansion in Cartesian coordinates as the following equations:

$$V(r) = V(0) + \left[\left(\frac{\partial V}{\partial x_i}\right)\Big|_0 \cdot x_i\right] + \frac{1}{2}\left[\left(\frac{\partial^2 V}{\partial x_i x_j}\right)\Big|_0 \cdot x_i x_j\right] + \cdots \quad (6)$$

Then, after simplification of the equation, there are only the second derivatives dependent on the same variable for the potential energy [65,66]:

$$U = -\frac{1}{2}\int_{\mathcal{D}} d^3\, r\, \rho_r \left[\left(\frac{\partial^2 V}{\partial x_i^2}\right)\Big|_0 \cdot x_i^2\right] = -\frac{1}{2}\int_{\mathcal{D}} d^3\, r\, \rho_r \left[\left(\frac{\partial E_i}{\partial x_i}\right)\Big|_0 \cdot x_i^2\right] =$$

$$-\frac{1}{2}\left(\frac{\partial E_i}{\partial x_i}\right)\Big|_0 \cdot \int_{\mathcal{D}} d^3\, r\, [\rho(r).x_i^2] \quad (7)$$

There are two parameters that must be obtained from NQR experiments; the quadrupole coupling constant, χ, and the asymmetry parameter of the EFG tensor η:

$$\chi = {e^2 Q q_{zz}}/{h} \quad (8)$$

$$\eta = {q_{xx} - q_{yy}}/{q_{zz}} \quad (9)$$

where q$_{ii}$ are components of the EFG tensor at the quadrupole nucleus determined in the EFG principal axes system, Q is the nuclear quadrupole moment, e is the proton charge, and h is Planck's constant [67]. In this article, the electric potential as the amount of work energy through transferring the electric charge from one site to another site in the presence of an electric field has been measured for benzotriazole, 2-mercaptobenzothiazole, 8-hydroxyquinoline, and 3-amino-1, 2, 4-triazole-5-thiol diffusing onto Al-Mg-Ge alloy surface using CAM-B3LYP/EPR-III, LANL2DZ,6-31+G(d,p) level of theory (Table 3).
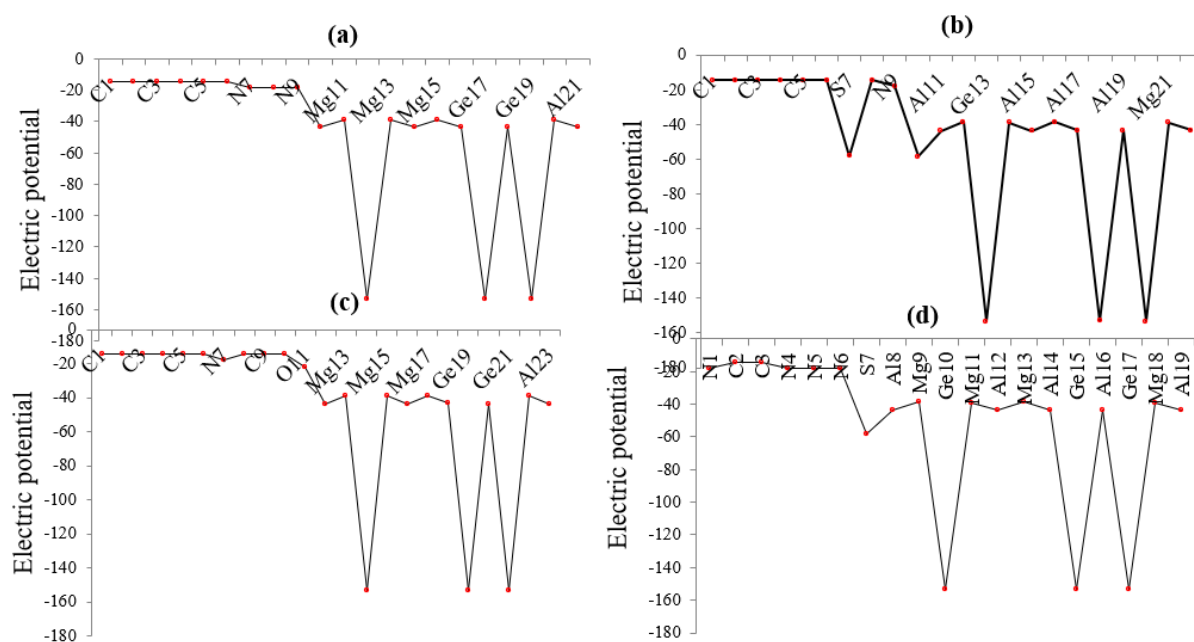
Table 3. The electric potential for elements of benzotriazole, 2-mercaptobenzothiazole, 8- hydroxyquinoline, and 3-amino-1, 2, 4-triazole-5-thiol adsorbed on the Al-Mg-Ge alloy surface by CAM-B3LYP/EPR-III,6-31+G(d,p) calculation extracted of NQR method.

Atom type	Benzotriazole	Atom type	2-mercapto benzothiazole	Atom type	8- hydroxy quinoline	Atom type	3-amino-1, 2, 4- triazole-5- thiol
C1	-14.608	C1	-14.5565	C1	-14.5023	N1	-18.1767
C2	-14.5703	C2	-14.5661	C2	-14.5705	C2	-14.4829
C3	-14.5289	C3	-14.5610	C3	-14.5345	C3	-14.5442
C4	-14.5392	C4	-14.5307	C4	-14.5517	N4	-18.0438
C5	-14.56	C5	-14.5668	C5	-14.5797	N5	-18.1656
C6	-14.5726	C6	-14.5674	C6	-14.5630	N6	-18.0478
N7	-18.1125	S7	-58.2734	N7	-18.1266	S7	-58.3439
N8	-18.082	C8	-14.5668	C8	-14.5341	Al8	-43.7076
N9	-18.0927	N9	-18.1306	C9	-14.5634	Mg9	-38.6585
Al10	-43.6896	S10	-58.4401	C10	-14.5582	Ge10	-153.2691
Mg11	-38.6588	Al11	-43.7066	O11	-22.0585	Mg11	-38.9054
Ge12	-153.254	Mg12	-38.6508	Al12	-43.7008	Al12	-43.7145
Mg13	-38.8931	Ge13	-153.2729	Mg13	-38.6711	Mg13	-38.6323
Al14	-43.6839	Mg14	-38.9232	Ge14	-153.2765	Al14	-43.1925
Mg15	-38.6711	Al15	-43.7015	Mg15	-38.9118	Ge15	-153.0147
Al16	-43.2132	Mg16	-38.6822	Al16	-43.7029	Al16	-43.5003
Ge17	-152.998	Al17	-43.2317	Mg17	-38.6737	Ge17	-153.2717
Al18	-43.5158	Ge18	-153.0215	Al18	-43.2118	Mg18	-38.9177
Ge19	-153.256	Al19	-43.5320	Ge19	-153.0058	Al19	-43.5190
Mg20	-38.88	Ge20	-153.2776	Al20	-43.5138		
Al21	-43.5287	Mg21	-38.9149	Ge21	-153.2800		
		Al22	-43.5314	Mg22	-38.9192		
				Al23	-43.5200		

The electric potential $(J \cdot C^{-1})$ is a continuous function in space produced by an idealized point charge that has $1/r$ potential: $V_E = \frac{1}{4\pi\varepsilon_0}\frac{Q}{r}$, where Q (measured in coulombs) is the point charge, r is the distance from the charge and ε_0 is the permittivity of a vacuum.

Since the electric potential for a system of point charges is equal to the sum of the point charges' individual potentials, the calculations are done simply based on the summation of potential fields, which is scalar instead of the summation of the electric fields, which is vector and much more difficult that potential field. So, $V_E(r) = \frac{1}{4\pi\varepsilon_0}\sum_i \frac{q_i}{|r-r_i|}$, where r is the point at which the potential is measured, r_i is a point at which the charge is $\neq 0$, and q_i is the charge at the point r_i. Finally, the potential of a continuous charge distribution $\rho(r)$ appears: $V_E(r) = \frac{1}{4\pi\varepsilon_0}\int_R \frac{\rho(r')}{|r-r'|}d^3r'$, where R is a region including all the points at which the charge density is $\neq 0$, r' is a point inside R, and $\rho(r')$ is the charge density at the point r' [68].

In addition, in Figure5a-d, it has been plotted the electric potential of the NQR method for elements of benzotriazole, 2-mercaptobenzothiazole, 8- hydroxyquinoline, and 3-amino-1, 2, 4-triazole-5-thiol that have been adsorbed on the Al-Mg-Ge alloy surface using CAM-B3LYP/EPR-III, LANL2DZ,6-31+G(d,p) level of theory.

Figure 5. The electric potential versus atom number through NQR calculation for **(a)** benzotriazole, **(b)** 2-mercaptobenzothiazole, **(c)** 8- hydroxyquinoline, and **(d)** 3-amino-1, 2, 4-triazole-5-thiol adsorbing on the Al-Mg-Ge alloy surface using CAM-B3LYP/EPR-III, LANL2DZ,6-31+G(d,p).

Therefore, it has been observed the effect of the substitution of aluminum atoms in the Al-Al surface with magnesium and germanium in the aluminum alloy (Al-Mg-Ge) resulted from electric potential using NQR analysis (Figure 5). It is obvious that the graph of Al-Al is fluctuated by Mg and Ge atoms in the related alloy. In Figure 5, it has been remarked the changes of electric potential for carbon, nitrogen, oxygen, sulfur, aluminum, magnesium, and germanium in benzotriazole → Al-Mg-Ge, 2-mercaptobenzothiazole→ Al-Mg-Ge, 8-hydroxyquinoline → Al-Mg-Ge, and 3-amino-1, 2, 4-triazole-5-thiol → Al-Mg-Ge.

3.4. Charge density analysis.

Through observing the intra/inter interactions between organic inhibitors of benzotriazole, 2-mercaptobenzothiazole, 8- hydroxyquinoline, and 3-amino-1, 2, 4-triazole-5-thiol with Al-Mg-Ge alloy surface and consequently the formation of adsorbed surfaces of benzotriazole → Al-Mg-Ge, 2-mercaptobenzothiazole→ Al-Mg-Ge, 8- hydroxyquinoline → Al-Mg-Ge, and 3-amino-1, 2, 4-triazole-5-thiol → Al-Mg-Ge (Tables 2) based on Langmuir adsorption using CAM-B3LYP/6-31+G(d,p)/EPR-III/LANL2DZ level of theory, CDD (the charge density difference) for these structures at the adsorption site has been estimated and plotted in Figure 6 with the following equation:

$$\Delta Q_{ads} = Q_{inhibitor\rightarrow[Al-Mg-Ge]\,surface} - (Q_{inhibitor} + Q_{[Al-Mg-Ge]\,surface}) \quad (10)$$

where $Q_{inhibitor\rightarrow[Al-Mg-Ge]\,surface}$ is the charge density of the adsorption system; $Q_{inhibitor}$ and $Q_{[Al-Mg-Ge]surface}$ are the charge densities of non-interacting of organic inhibitor and that of the Al-Mg-Ge alloy surface.

3.5. Potential energy of interatomic interaction.

The interatomic potential explains the interaction between a pair of atoms or the interaction of an atom with a group of atoms in a condensed phase. When binding happens, we can observe the potential to have both an attractive and a repulsive component [69-74].
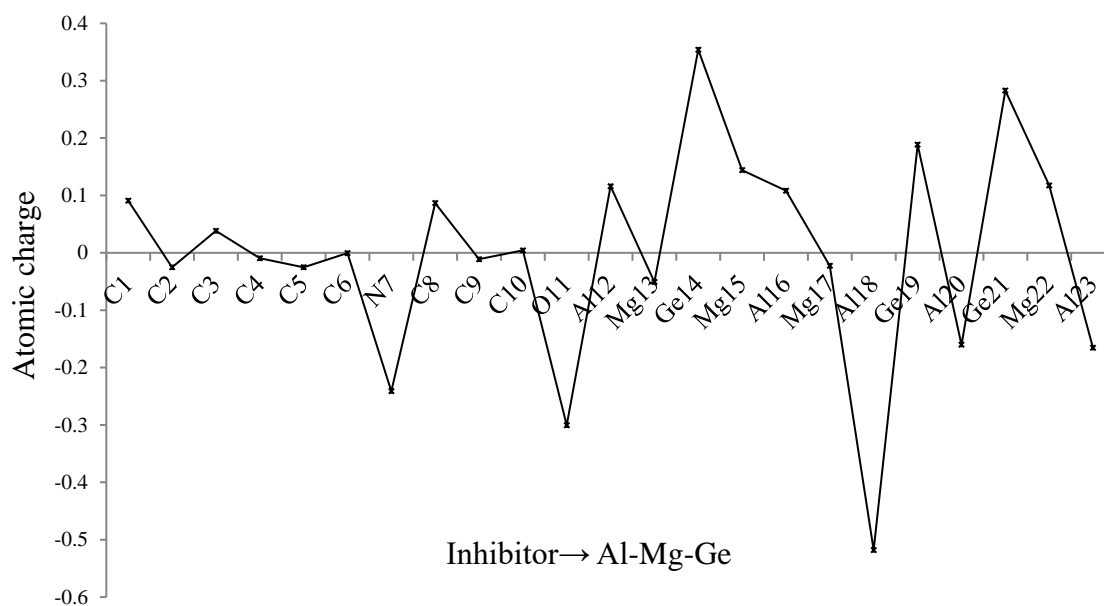
Figure 6. The calculated electronic charge for aluminum atom through intra-atomic interaction with magnesium and germanium in the alloy surface of [Al-Mg-Ge] and through interatomic interaction with organic inhibitors in the adsorption site (N→ Al, O→Al, S→Al) calculated by the level of theory CAM-B3LYP/6-31+G (d,p)/EPR-III/LANL2DZ.

The figure of the potential energy as a function of lattice distance with the interval of interatomic interaction in a solid is described as an atom in the ideal crystalline solid feeling the same potential through the other atoms in the material. Accompanying the equation (15), it has been investigated the Morse potential, which is applied for molecular vibrations and solids [75] and also excited the functional form of more accurate potentials like the bond-order potentials:

$$V_{\mathrm{M}}\ (r) = \ D_e\ (e^{-2\alpha(r-r_e)}\ - 2e^{-\alpha(r-r_e)}) \qquad (11)$$

where D_e is the equilibrium bond energy and r_e the bond distance. Therefore, the optimized potential energy of interatomic interaction for benzotriazole → Al-Mg-Ge, 2-mercaptobenzothiazole→ Al-Mg-Ge, 8- hydroxyquinoline → Al-Mg-Ge, and 3-amino-1, 2, 4-triazole-5-thiol → Al-Mg-Ge have been measured (Table4).

Table 4. Potential energy (kcal/mol) of interatomic interaction and distance (Å) of the nitrogen atom in benzotriazole, the oxygen atom in 8- hydroxyquinoline, and the sulfur atom in both 2-mercaptobenzothiazole and 3-amino-1, 2, 4-triazole-5-thiol, respectively, with aluminum in Al-Mg-Ge nanosurface.

Compound	Potential energy×10⁻⁴ (kcal/mol)	Distance	(Å)
Al-Mg-Ge	-512.9296	-	-
Benzotriazole	-24.5172	-	-
Benzotriazole → Al-Mg-Ge	-534.6512	N $_{inhibitor}$ → Al $_{surface}$	1.9470
2-mercaptobenzothiazole	-69.5235	-	-
2-mercaptobenzothiazole→ Al-Mg-Ge	-579.6410	S $_{inhibitor}$ → Al $_{surface}$	2.1001
8- hydroxyquinoline	-29.5527	-	-
8- hydroxyquinoline → Al-Mg-Ge	-539.6983	O $_{inhibitor}$ → Al $_{surface}$	1.9098
3-amino-1, 2, 4-triazole-5-thiol	-43.1337	-	-
3-amino-1, 2, 4-triazole-5-thiol → Al-Mg-Ge	-553.2601	S $_{inhibitor}$ → Al $_{surface}$	2.20011

Then, the distance between the nitrogen atom in benzotriazole, the oxygen atom in 8-hydroxyquinoline, and the sulfur atom in 2-mercaptobenzothiazole and 3-amino-1, 2, 4-triazole-5-thiol, respectively, with aluminum in Al-Mg-Ge nanosurface has been evaluated (Table 4). Finally, the changes in potential energy for these complexes and interatomic integration distance have been plotted in Figure 7.
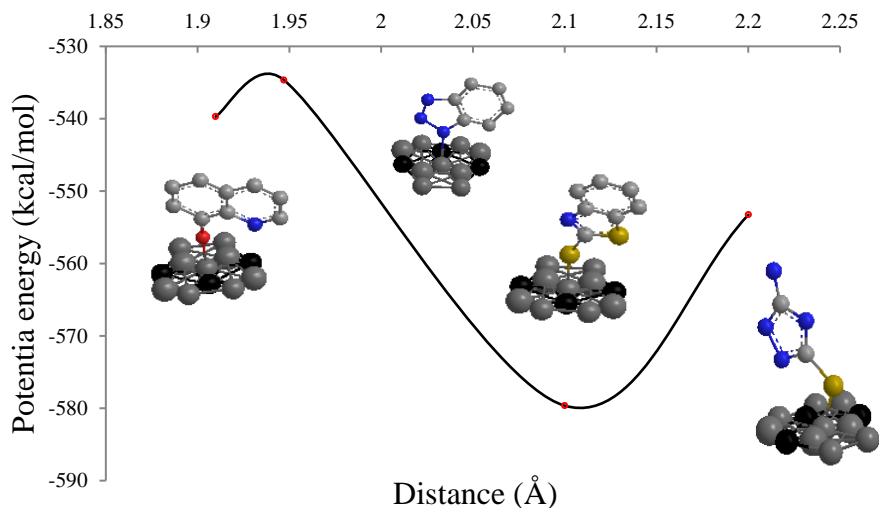
Figure 7. The graph of potential energy (kcal/mol) of interatomic interaction versus distance (Å) of the nitrogen atom in benzotriazole, the oxygen atom in 8- hydroxyquinoline, and the sulfur atom in both 2-mercaptobenzothiazole and 3-amino-1, 2, 4-triazole-5-thiol, respectively, with aluminum in Al-Mg-Ge nanosurface.

Based on Figure 7, it can be assumed that for benzotriazole → Al-Mg-Ge, 2-mercaptobenzothiazole→ Al-Mg-Ge, 8- hydroxyquinoline → Al-Mg-Ge, and 3-amino-1, 2, 4-triazole-5-thiol → Al-Mg-Ge, Lennar Jones potential as an intermolecular pair potential can be described [76]:

$$V_{LJ}(r) = 4\varepsilon \left[\left(\frac{\sigma}{r} \right)^{12} - \left(\frac{\sigma}{r} \right)^{6} \right] \qquad (12)$$

where ε is the depth of the potential well and σ is the interval at which the potential=0. The attractive term is proportional to $\frac{1}{r^6}$ in the potential comes from balancing the van der Waals forces, while the $\frac{1}{r^{12}}$ repulsive term is much more approximate [77].

3.6. HOMO, LUMO and UV-VIS analysis.

The ionization causes the highest occupied molecular orbital "HOMO" energy, and the electron affinity produces the lowest unoccupied molecular orbital "LUMO" energy which has been calculated and reported for benzotriazole → Al-Mg-Ge, 2-mercaptobenzothiazole → Al-Mg-Ge, 8- hydroxyquinoline → Al-Mg-Ge, and 3-amino-1, 2, 4-triazole-5-thiol → Al-Mg-Ge in Scheme 3. The HOMO (au), LUMO (au), and band energy gap ($\Delta E = E_{LUMO} - E_{HOMO}$) (ev) presented the pictorial explanation of the frontier molecular orbital and their respective positive and negative zones, which are an important factor for identifying the molecular characteristics of effective compounds in these organic inhibitors (Scheme 3).
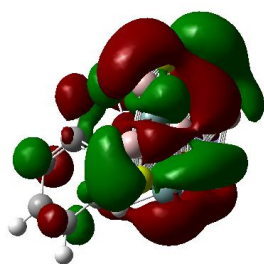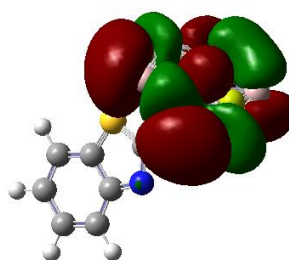
(a)
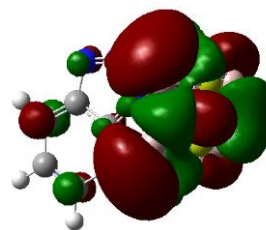
HOMO benzotriazole → Al-Mg-Ge = -0.0324

ΔE= 1.6403

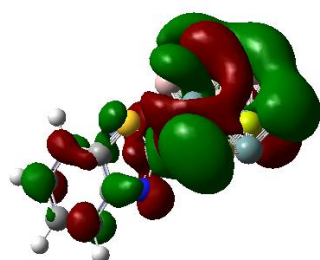LUMO benzotriazole → Al-Mg-Ge = 0.0278

(b)

HOMO mercaptobenzothiazole→ Al-Mg-Ge = -0.0890

ΔE= 3.2096

LUMO mercaptobenzothiazole→ Al-Mg-Ge = 0.0289

(c)

HOMO $_{8\text{-hydroxyquinoline}} \rightarrow$ Al-Mg-Ge = -0.0194

ΔE= 1.5431

LUMO $_{8\text{-hydroxyquinoline}} \rightarrow$ Al-Mg-Ge = 0.0372

(d)

HOMO $_{3\text{-amino-1, 2, 4-triazole-5-thiol}} \rightarrow$ Al-Mg-Ge = 0.0453

ΔE= 2.0299

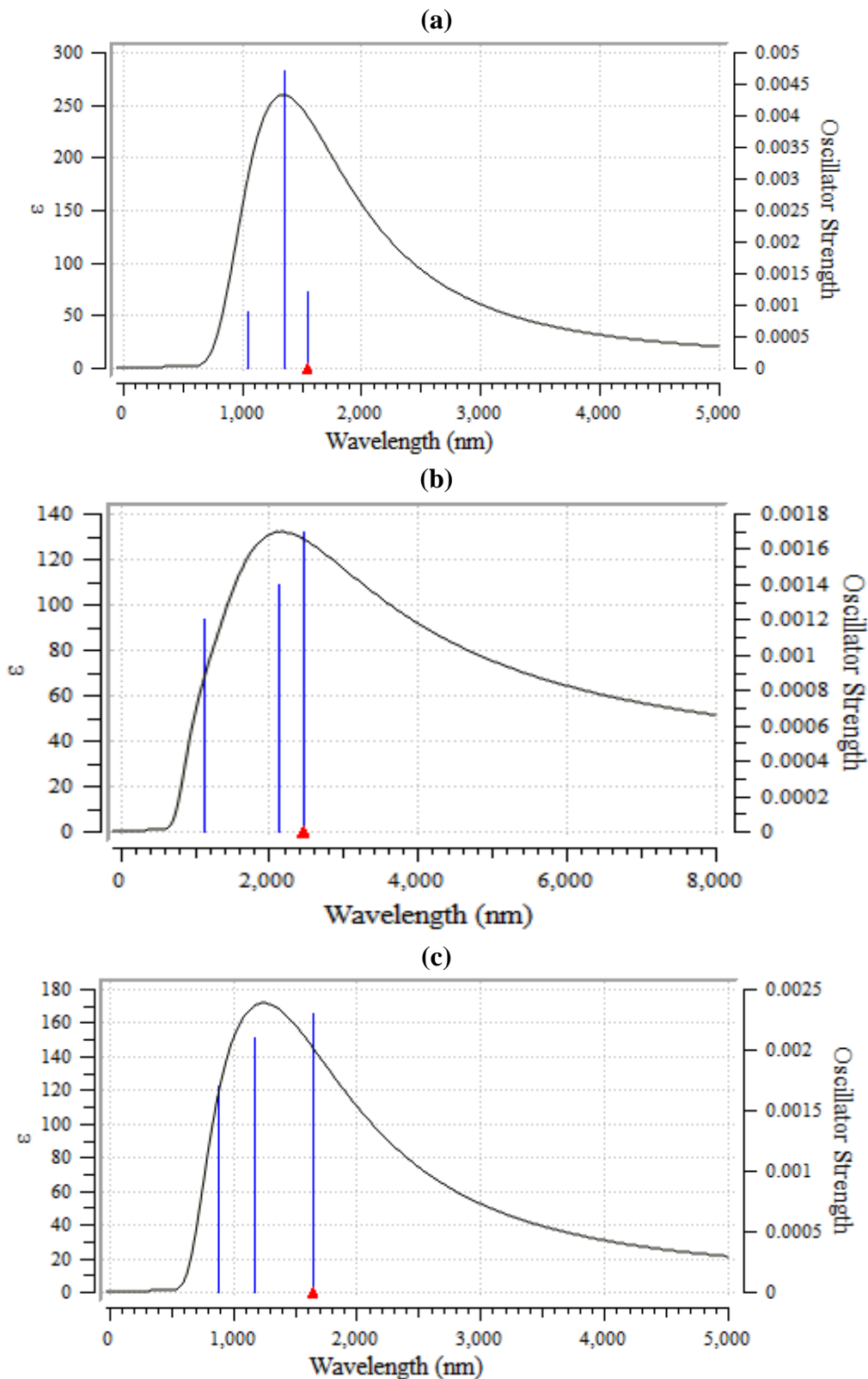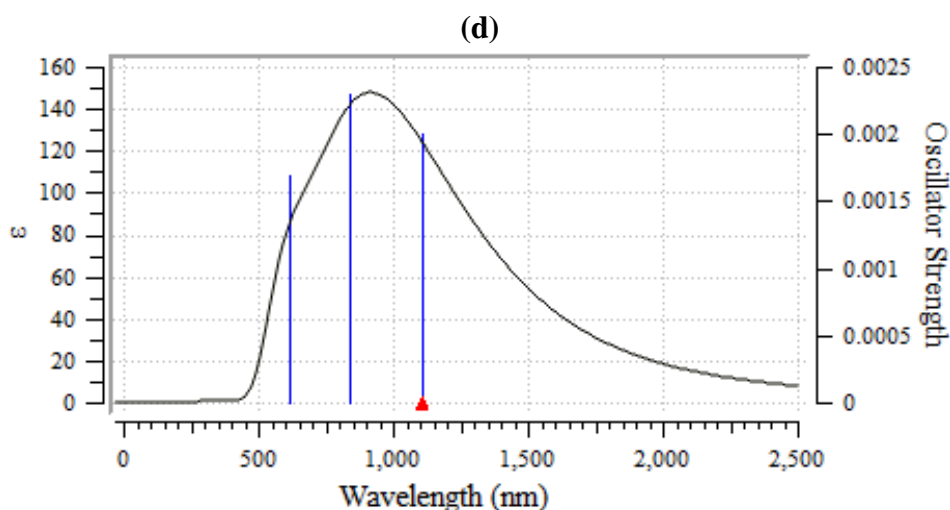LUMO $_{3\text{-amino-1, 2, 4-triazole-5-thiol}} \rightarrow$ Al-Mg-Ge = -0.0293
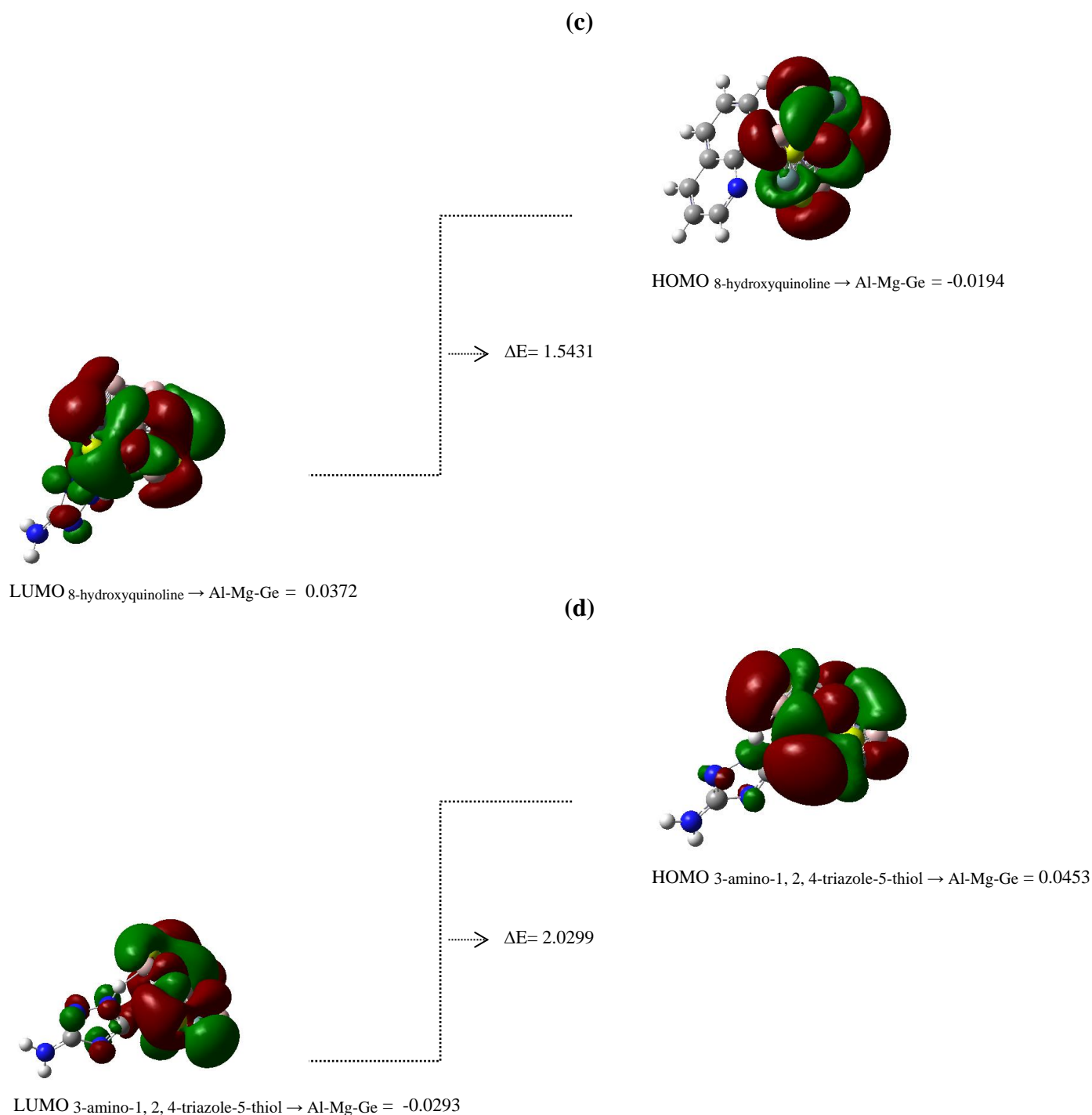
Scheme 3. The HOMO (au), LUMO(au) and band energy gap (ev) for three organic inhibitors for **(a)** benzotriazole $\rightarrow$ Al-Mg-Ge, **(b)** 2-mercaptobenzothiazole, **(c)** 8-hydroxyquinoline and **(d)** 3-amino-1, 2, 4-triazole-5-thiol $\rightarrow$ Al-Mg-Ge.

On the other hand, the HOMO shows the capability for giving an electron while the LUMO as an electron acceptor, exhibits the capability for achieving an electron. Therefore, the energy gap (ΔE = E $_{\text{LUMO}}$-E$_{\text{HOMO}}$) indicates the energy difference between frontier HOMO and LUMO orbital introducing the structure's stability and unraveling the molecule's chemical activity. In this work, the energy gap establishes how benzotriazole, 8-hydroxyquinoline, 2-mercaptobenzothiazole, and 3-amino-1, 2, 4-triazole-5-thiol adsorb on the Al-Mg-Ge alloy surface at CAM-B3LYP/6-311+G(2d,p)/EPR-III/LANL2DZ quantum method. Besides, frontier molecular orbitals run an important function in the optical and electrical properties like in UV-VIS spectra [78].

The energy gap between HOMO and LUMO has distinguished the attributes of molecular electrical transport [79-84]. Through the Frank–Condon principle, the maximum absorption peak (max) depends on a UV–visible spectrum to vertical excitation.

In this verdict, TD-DFT/6-31+G (2d, p)/EPR-III/LANL2DZ computations have been done to identify the low-lying excited states of benzotriazole, 8-hydroxyquinoline, 2-mercaptobenzothiazole and 3-amino-1, 2, 4-triazole-5-thiol adsorbing on the Al-Mg-Ge alloy surface. The results consist of the vertical excitation energies, oscillator strength, and wavelength introduced in Figure 8 a-d.

(a)

(b)

(c)

(d)

Figure 8. UV-VIS spectra for **(a)** benzotriazole → Al-Mg-Ge, **(b)** 2-mercaptobenzothiazole, **(c)** 8-hydroxyquinoline and **(d)** 3-amino-1, 2, 4-triazole-5-thiol → Al-Mg-Ge.

Based on the computed amounts of UV-VIS spectra for benzotriazole, 2-mercaptobenzothiazole, 8-hydroxyquinoline, and 3-amino-1, 2, 4-triazole-5-thiol adsorbing on the Al-Mg-Ge alloy surface, there are maximum adsorption bands between 500 nm-2000 nm wavelengths for these organic heterocyclic inhibitors joint metal alloy which has remarked a sharp peak with approximately 1000 nm wavelength (Figure 8a-d).

4. Conclusions

In this research, the adsorption and diffusion of benzotriazole, 2-mercaptobenzothiazole, 8-hydroxyquinoline, and 3-amino-1, 2, 4-triazole-5-thiol adsorbing on the Al-Mg-Ge alloy surface have been investigated based on Langmuir theory using ONIOM method with high, medium and low levels of EPR-III/6-31+G (d,p)/LANL2DZ, semi-empirical and MM2 basis sets, respectively by program package Gaussian 16 revision C.01.

In this work, the efficiency of the organic inhibitors as the aluminum alloy coating has been studied through the electronic, thermodynamic features and characteristics of the environmental condition, which results in the complexes of benzotriazole → Al-Mg-Ge, 2-mercaptobenzothiazole→ Al-Mg-Ge, 8- hydroxyquinoline → Al-Mg-Ge, and 3-amino-1, 2, 4-triazole-5-thiol → Al-Mg-Ge.

An elaborate investigation for the mechanism of local minima in the adsorption potential energy landscape represents that the intact benzotriazole, 2-mercaptobenzothiazole, 8-hydroxyquinoline, and 3-amino-1, 2, 4-triazole-5-thiol have been adsorbed with the aromatic ring parallel to the Al-Mg-Ge alloy surface. In the preferred path, these organic inhibitors remain parallel to the surface while performing small single rotational steps with a carbon-carbon double bond hinged above a single Al atom.

Conflicts of Interest

The authors declare no conflict of interest.

References

1. Bai,G.; Tian, J.; Qingwei Guo, Li,Z.; Yuhong Zhao,Y. First Principle Study on Mg2X (X = Si, Ge, Sn) Intermetallics by Bi Micro-Alloying. *Crystals* **2021**, *11*, 142, https://doi.org/10.3390/cryst11020142.

2. Norder, J.; George, R.; Butcher, C.; Worswick, M.J. Friction characterization and application to warm forming of a high strength 7000-series aluminum sheet. *J. Mater. Process. Technol.* **2021**, *293*, 117066, https://doi.org/10.1016/j.jmatprotec.2021.117066

3. Monajjemi, M.; Mahdavian, L.; Mollaamin, F.; Khaleghian, M. Interaction of Na, Mg, Al, Si with carbon nanotube (CNT): NMR and IR study. *Russ. J. Inorg. Chem* **2009**, *54*, 1465-1473, https://doi.org/10.1134/S0036023609090216.

4. Yu, P.; Wu, C.; Shi, L. Analysis and characterization of dynamic recrystallization and grain structure evolution in friction stir welding of aluminum plates. *Acta Mater.* **2021**, *207*, 116692, https://doi.org/10.1016/j.actamat.2021.116692.

5. Meng, X.; Huang, Y.; Cao, J.; Shen, J.; dos Santos, J.F. Recent progress on control strategies for inherent issues in friction stir welding. *Prog. Mater. Sci.* **2021**, *115*, 100706, https://doi.org/10.1016/j.pmatsci.2020.100706.

6. Hua, L.; Zhang, W.; Ma, H.; Hu, Z. Investigation of formability, microstructures and post-forming mechanical properties of heat-treatable aluminum alloys subjected to pre-aged hardening warm forming. *Int. J. Mach. Tool. Manuf.* **2021**, *169*, 103799, https://doi.org/10.1016/j.ijmachtools.2021.103799.

7. Xu, W.; Zhang, B.; Li, X.Y.; Lu, K. Suppressing atomic diffusion with the Schwarz crystal structure in supersaturated Al-Mg alloys. *Science* **2021**, *373*, 683–687, https://doi.org/10.1073/pnas.1319436111.

8. Zhu, L.X.; Zou, M.S.; Zhang, X.D.; Zhang, L.C.; Wang, X.X.; Song, T.L.; Wang, S.; Li, X.D. Enhanced Hydrogen Generation Performance of Al-Rich Alloys by a Melting-Mechanical Crushing-Ball Milling Method. *Materials* **2021**, *14*, 7889, https://doi.org/10.3390/ma14247889.

9. Qiang,Y.; Guo,L.; Li,H.; Lan,X. Fabrication of environmentally friendly Losartan potassium film for corrosion inhibition of mild steel in HCl medium. *Chemical Engineering Journal.* **2021**, *406*, 126863, https://doi.org/10.1016/j.cej.2020.126863.

10. Zhu, Z.; Ng, F.L.; Seet, H.L.; Lu, W.; Liebscher, C.H.; Rao, Z.; Raabe, D.; Ling Nai, S.M. Superior mechanical properties of a selective-laser-melted AlZnMgCuScZr alloy enabled by a tunable hierarchical microstructure and dual-nanoprecipitation. *Mater. Today* **2021**, *52*, 90–101, https://doi.org/10.1016/j.mattod.2021.11.019.

11. Du, Z.H.; Deng, Z.S.; Cui, X.H.; Xiao, A. Deformation Behavior and Properties of 7075 Aluminum Alloy under Electromagnetic Hot Forming. *Materials* **2021**, *14*, 4954, https://doi.org/10.3390/ma14174954.

12. Al-Amiery, A.A. Anticorrosion performance of 2-isonicotinoyl-n-phenylhydrazinecarbothioamide for mild steel hydrochloric acid solution: Insights from experimental measurements and quantum chemical calculations. *Surf. Rev. Lett.* **2021**, *28*, 2050058, https://doi.org/10.1142/S0218625X20500584.

13. Rogachev, S.O.; Naumova, E.A.; Vasileva, E.S.; Sundeev, R. Al-Ca, Al-Ce, and Al-La Eutectic Aluminum Alloys Processed by High-Pressure Torsion. A*dv. Eng. Mater.* **2021**, *24*, 2100772, https://doi.org/10.1002/adem.202100772.

14. Kokalj, A.; Lozinšek, M.; Kapun, B.; Taheri, P.; Neupane, S.; Losada-Pérez, P.; Xie, C.; Stavber, S.; Crespo, D.; Renner, F.U.; et al. Simplistic correlations between molecular electronic properties and inhibition efficiencies: Do they really exist? *Corros. Sci.* **2021**, *179*, 108856, https://doi.org/10.1016/j.corsci.2020.108856.

15. Neupane, S.; Losada-Pérez, P.; Tiringer, U.; Taheri, P.; Desta, D.; Xie, C.; Crespo, D.; Mol, A.; Milošev, I.; Kokalj, A.; et al. Study of Mercaptobenzimidazoles As Inhibitors for Copper Corrosion: Down to the Molecular Scale. *J. Electrochem. Soc.* **2021**, *168*, 051504, https://doi.org/10.1149/1945-7111/abf9c3.

16. Al-Baghdadi, S.B.; Al-Amiery, A.A.; Gaaz, T.S.; Kadhum, A.A.H. Terephthalohydrazide and isophthalo-hydrazide as new corrosion inhibitors for mild steel in hydrochloric acid: Experimental and theoretical approaches. *Koroze Ochr. Mater.* **2021**, *65*, 12–22, https://doi.org/10.2478/kom-2021-0002.

17. Schiessler, E.J.; Würger, T.; Lamaka, S.V.; Meißner, R.H.; Cyron, C.J.; Zheludkevich, M.L.; Feiler, C.; Aydin, R.C. Predicting the inhibition efficiencies of magnesium dissolution modulators using sparse machine learning models. *NPJ Comput. Mater.* **2021**, *7*, 1–9, https://doi.org/10.1038/s41524-021-00658-7.

18. Sousa, T.; Correia, J.; Pereira, V.; Rocha, M. Generative Deep Learning for Targeted Compound Design. *J. Chem. Inf. Model.* **2021**, *61*, 5343–5361, https://doi.org/10.1021/acs.jcim.0c01496.

19. Blanco, D.; Rubio, E.M.; Lorente-Pedreille, R.M.; Sáenz-Nuño, M.A. Sustainable Processes in Aluminium, Magnesium, and Titanium Alloys Applied to the Transport Sector: A Review. *Metals* **2021**, *12*, 9, https://doi.org/10.3390/met12010009.

20. Ma, L.; Qiang, Y.; Zhao, W. Designing Novel Organic Inhibitor Loaded MgAl-LDHs Nanocontainer for Enhanced Corrosion Resistance. *Chem. Eng. J.* **2021**, *408*, 127367, https://doi.org/10.1016/j.cej.2020.127367.

21. Oh, Y.; Han, C.H.; Wang, M.; Chun, Y.-B.; Han, H.N. Effect of Rare Earth Oxide Addition on Microstructure and Mechanical Properties of Ni-Based Alloy. *J. Alloy. Compd.* **2021**, *853*, 156980, https://doi.org/10.1016/j.jallcom.2020.156980.

22. Li, D.; Sun, L.; Hu, L.; Zhu, J.; Shi, J.; Guo, D. Rare Earth Insitu-Doped ZIF-67 Derived N Doped C Encapsulated Sm2O3/Co Nanoparticles as Excellent Oxygen Reduction Reaction Catalyst for Al-Air Batteries. *J. Power Sources* **2021**, *482*, 229052, https://doi.org/10.1016/j.jpowsour.2020.229052.

23. Chaubey, N.; Savita; Qurashi, A.; Chauhan, D.S.; Quraishi, M.A. Frontiers and advances in green and sustainable inhibitors for corrosion applications: A critical review. *J. Mol. Liq.* **2021**, *321*, 114385, https://doi.org/10.1016/j.molliq.2020.114385.

24. Mollaamin,F. Physicochemical investigation of anti-COVID19 drugs using several medicinal plants, *J. Chil. Chem. Soc.*, **2022**, *67*(2), 5537-5546. http://dx.doi.org/10.4067/S0717-97072022000205537

25. Mercado, R.; Rastemo, T.; Lindelöf, E.; Klambauer, G.; Engkvist, O.; Chen, H.; Jannik Bjerrum, E. Graph networks for molecular design. Mach. *Learn. Sci. Technol.* **2021**, *2*, 025023, https://doi.org/10.1088/2632-2153/abcf91.

26. Kumari, D.; Venugopal, P.P.; Kumari P. D., R.; Chakraborty, D. Exploring the potential role of quercetin in corrosion inhibition of aluminium alloy 6063 in hydrochloric acid solution by experimental and theoretical studies. *J. Adhes. Sci. Technol.* **2021**, https://doi.org/10.1080/01694243.2021.1999703.

27. Mollaamin, F. Chemotherapy study of alkaloids through theoretical quantum methods.*Moroccan Journal of Chemistry*.**2020**, *8*, 400-411, https://doi.org/10.48317/IMIST.PRSM/morjchem-v8i2.16604.

28. Nochebuena, J.; Naseem-Khan, S.; Cisneros, G. A. Development and application of quantum mechanics/molecular mechanics methods with advanced polarizable potentials, *WIREs Comput. Mol. Sci.* **2021**, *11*, e1515, https://doi.org/10.1002/wcms.1515.

29. Dennington, R.; Keith, T.A.; Millam, J.M. *GaussView*, Version 6, .Semichem Inc., Shawnee Mission, KS, **2016**, https://gaussian.com/citation/.

30. Frisch, M. J.; Trucks, G. W.; Schlegel, H. B.; Scuseria, G. E.; Robb, M. A.; Cheeseman, J. R.; Scalmani, G.; Barone, V.; Petersson, G. A.; Nakatsuji, H.; Li, X.; Caricato, M.; Marenich, A. V.; Bloino, J.; Janesko, B. G.; Gomperts, R.; Mennucci, B.; Hratchian, H. P.; Ortiz, J. V.; Izmaylov, A. F.; Sonnenberg, J. L.; Williams-Young, D.; Ding, F.; Lipparini, F.; Egidi, F.; Goings, J.; Peng, B.; Petrone, A.; Henderson, T.; Ranasinghe, D.; Zakrzewski, V. G.; Gao, J.; Rega, N.; Zheng, G.; Liang, W.; Hada, M.; Ehara, M.; Toyota, K.; Fukuda, R.; Hasegawa, J.; Ishida, M.; Nakajima, T.; Honda, Y.; Kitao, O.; Nakai, H.; Vreven, T.; Throssell, K.; Montgomery, J. A., Jr.; Peralta, J. E.; Ogliaro, F.; Bearpark, M. J.; Heyd, J. J.; Brothers, E. N.; Kudin, K. N.; Staroverov, V. N.; Keith, T. A.; Kobayashi, R.; Normand, J.; Raghavachari, K.; Rendell, A. P.; Burant, J. C.; Iyengar, S. S.; Tomasi, J.; Cossi, M.; Millam, J. M.; Klene, M.; Adamo, C.; Cammi, R.; Ochterski, J. W.; Martin, R. L.; Morokuma, K.; Farkas, O.; Foresman, J. B.; Fox, D. J. Gaussian 16, Revision C.01, *Gaussian*, Inc., Wallingford CT, **2016**, https://gaussian.com/citation/.

31. Tian, G.; Du, H.; Zhang, H. First Principle Analysis on Pyridine Amide Derivatives' Adsorption Behavior on the Pt (111) Surface. *Crystals* **2021**, *11*, 98, https://doi.org/10.3390/cryst11020098.

32. Mandal, S.; Calderon, J.; Marpu, S.B.; Omary, M.A.; Shi, S.Q. Mesoporous activated carbon as a green adsorbent for the removal of heavy metals and Congo red: Characterization, adsorption kinetics, and isotherm studies. *J. Contam. Hydrol.* **2021**, *243*, 103869, https://doi.org/10.1016/j.jconhyd.2021.103869.

33. Monajjemi, M.; Mollaamin, F.; Gholami, M.R.; Yoosbashizadeh, H.; Sadrnezhad, S.K.; Passdar, H. Quantum Chemical Parameters of Some Organic Corrosion Inhibitors, Pyridine, 2-Picoline 4-Picoline and 2,4-Lutidine, Adsorption at Aluminum Surface in Hydrochloric and Nitric Acids and Comparison Between Two Acidic Media. *Main Group Met. Chem.* **2003**, *26*, 349-362, https://doi.org/10.1515/MGMC.2003.26.6.349.

34. Mollaamin, F., Monajjemi, M. Transition metal (X = Mn, Fe, Co, Ni, Cu, Zn)-doped graphene as gas sensor for CO_2 and NO_2 detection: a molecular modeling framework by DFT perspective. *J Mol Model* **29**, 119 (2023). https://doi.org/10.1007/s00894-023-05526-3.

35. Mollaamin, F.; Monajjemi, M. Fractal Dimension on Carbon Nanotube-Polymer Composite Materials Using Percolation Theory. *Journal of Computational and Theoretical Nanoscience*.**2012**, *9*, 597-601, https://doi.org/10.1166/jctn.2012.2067.

36. Mollaamin, F.; Monajjemi, M.; Sakhaeinia, H. Nano-metallic Semiconductor towards the Vibrational Analysis and Harmonic Linear Combination. *Russ. J. Phys. Chem.***2022**, *96*, 1051–1061, https://doi.org/10.1134/S0036024422050090.

37. Bakhshi, K.; Mollaamin, F.; Monajjemi, M. Exchange and correlation effect of hydrogen chemisorption on nano V(100) surface: A DFT study by generalized gradient approximation (GGA). *J.Comput.Theor.Nanosci*, **2011**, *8*,763-768, https://doi.org/10.1166/jctn.2011.1750.

38. Mollaamin, F. Features of parametric point nuclear magnetic resonance of metals implantation on boron nitride nanotube by density functional theory/electron paramagnetic resonance. *Journal of Computational and Theoretical Nanoscience* **2014**, *11*, 2393-2398, https://doi.org/10.1166/jctn.2014.3653.

39. Khalili Hadad, B.; Mollaamin, F. Monajjemi, M. Biophysical chemistry of macrocycles for drug delivery: a theoretical study. *Russ Chem Bull* **2011**, *60*, 238, https://doi.org/10.1007/s11172-011-0039-5.

40. Monajjemi, M.; Khaleghian, M.; Tadayonpour, N.; Mollaamin, F. The effect of different solvents and temperatures on stability of single-walled carbon nanotube: A QM/MD study. *Int. J. Nanosci.* **2010**, *09*, 517-529, https://doi.org/10.1142/S0219581X10007071.

41. Mollaamin, F.; Ilkhani, A.; Sakhaei, N.; Bonsakhteh, B.; Faridchehr, A.; Tohidi, S.; Monajjemi, M., Thermodynamic and solvent effect on dynamic structures of nano bilayer-cell membrane: Hydrogen bonding study. *Journal of Computational and Theoretical Nanoscience* **2015**, *12*, 3148-3154, https://doi.org/10.1166/jctn.2015.4092.

42. Zadeh, M.A.A.; Lari, H.; Kharghanian, L.; Balali, E.; Khadivi, R.; Yahyaei, H.; Mollaamin, F.; Monajjemi, M. Density functional theory study and anti-cancer properties of shyshaq plant: In view point of nano biotechnology. *Journal of Computational and Theoretical Nanoscience* **2015**, *12*, 4358-4367, https://doi.org/10.1166/jctn.2015.4366.

43. Monajjemi, M.; Lee, V.S.; Khaleghian, M.; Honarparvar, B.; Mollaamin, F. Theoretical Description of Electromagnetic Nonbonded Interactions of Radical, Cationic, and Anionic NH2BHNBHNH2 Inside of the B18N18 Nanoring. *J. Phys. Chem C* **2010**, *114*, 15315-15330, https://doi.org/10.1021/jp104274z.

44. Becke, A.D. Density-functional thermochemistry. III. The role of exact exchange. *J Chem Phys* **1993**, *98*, 5648–5652, https://doi.org/10.1063/1.464913.

45. 45. Lee, C.; Yang,W.; Parr, R.G. Development of the Colle–Salvetti correlation-energy formula into a functional of the electron density. *Phys Rev B* **1988**, *37*, 785–789, http://dx.doi.org/10.1103/PhysRevB.37.785.

46. Shahriari, S.; Mollaamin, F.; Monajjemi, M. Increasing the Performance of {[(1-x-y) LiCo0.3Cu0.7] (Al and Mg doped)] O2}, xLi2MnO3, yLiCoO2 Composites as Cathode Material in Lithium-Ion Battery: Synthesis and Characterization. *Micromachines* **2023**, *14*, 241. https://doi.org/10.3390/mi14020241

47. Stephens, P.J.; Devlin, F.J.; Chabalowski, C.F.; Frisch, M. J. Ab Initio Calculation of Vibrational Absorption and Circular Dichroism Spectra Using Density Functional Force Fields. *J. Phys. Chem.* **1994**, *98,* 11623–11627, https://doi.org/10.1021/j100096a001.

48. Cramer, C.J. Essentials of Computational Chemistry: Theories and Models, 2nd Edition Wiley. **2004**.

49. Vosko, S. H.; Wilk, L.; Nusair,M. Accurate spin-dependent electron liquid correlation energies for local spin density calculations: a critical analysis. *Can. J. Phys.* **1980**, *58*, 1200–1211, https://doi.org/10.1139/p80-159.

50. Becke, A.D. Density-functional exchange-energy approximation with correct asymptotic behavior. *Phys. Rev. A* **1988**, *38*, 3098–3100, https://doi.org/10.1103/PhysRevA.38.3098.

51. Mollaamin, F. and Monajjemi, M. THERMODYNAMIC RESEARCH ON THE INHIBITORS OF CORONAVIRUS THROUGH DRUG DELIVERY METHOD. *J. Chil. Chem. Soc.* **2021**, *66*, 5195-5205. http://dx.doi.org/10.4067/S0717-97072021000205195.

52. Mollaamin, F.; Shahriari, S.; Monajjemi, M.; Khalaj,Z. Nanocluster of Aluminum Lattice via Organic Inhibitors Coating: A Study of Freundlich Adsorption. *J Clust Sci* **2022**, https://doi.org/10.1007/s10876-022-02335-1.

53. Mollaamin, F.; Monajjemi, M. Molecular modelling framework of metal-organic clusters for conserving surfaces: Langmuir sorption through the TD-DFT/ONIOM approach. *Mol Simul* **2023**, *49*, 365-376, https://doi.org/10.1080/08927022.2022.2159996.

54. Fry,R.A.; Kwon, K.D.; Komarneni, S.; Kubicki,J.D.; Mueller,K.T. Solid-State NMR and Computational Chemistry Study of Mononucleotides Adsorbed to Alumina. *Langmuir* **2006**, *22*, 9281-9286, https://doi.org/10.1021/la061561s.

55. Tahan, A.; Mollaamin, F.; Monajjemi, M. Thermochemistry and NBO analysis of peptide bond: Investigation of basis sets and binding energy. *Russian Journal of Physical Chemistry A* **2009**, *83*, 587-597, https://doi.org/10.1134/S003602440904013X.

56. Mollaamin, F.; Monajjemi, M. Harmonic Linear Combination and Normal Mode Analysis of Semiconductor Nanotubes Vibrations. *J. Comput. Theor. Nanosci* **2015**, *12*, 1030-1039, https://doi.org/10.1166/jctn.2015.3846.

57. Mollaamin, F.; Monajjemi, M.; Salemi, S.; Baei, M.T. A Dielectric Effect on Normal Mode Analysis and Symmetry of BNNT Nanotube. *Fuller. Nanotub. Carbon Nanostructures* **2011**, *19*, 182-196, https://doi.org/10.1080/15363831003782932.

58. Monajjemi, M.; Honaparvar, B.; Khalili Hadad, B.; Ilkhani, A.; Mollaamin, F. Thermo-Chemical Investigation and NBO Analysis of Some anxileotic as Nano- Drugs. *African journal of pharmacy and pharmacology* **2010**, *4*, 521-529.

59. Monajjemi, M.; Najafpour, J.; Mollaamin, F. (3,3)$_4$ Armchair carbon nanotube in connection with PNP and NPN junctions: Ab Initio and DFT-based studies. *Fullerenes Nanotubes and Carbon Nanostructures* **2013**, *21*, 213-232, https://doi.org/10.1080/1536383X.2011.597010.

60. Monajjemi, M.; Jafari Azan, M.; Mollaamin, F. Density functional theory study on B30N20 nanocage in structural properties and thermochemical outlook. *Fullerenes Nanotubes and Carbon Nanostructures* **2013**, *21*, 503-515, https://doi.org/10.1080/1536383X.2011.629762.

61. Monajjemi, M.; Baie, M.T.; Mollaamin, F. Interaction between threonine and cadmium cation in [Cd(Thr)] (n = 1-3) complexes: Density functional calculations , *Russian Chemical Bulletin*, **2010**, *59*, 886-889, https://doi.org/10.1007/s11172-010-0181-5.

62. Monajjemi, M.; Baheri, H.; Mollaamin, F. A percolation model for carbon nanotube-polymer composites using the Mandelbrot-Given. *Journal of Structural Chemistry* **2011**, *52*, 54-59, https://doi.org/10.1134/S0022476611010070.

63. Sarasia, E.M.; Afsharnezhad, S.; Honarparvar, B.; Mollaamin, F.; Monajjemi, M. Theoretical study of solvent effect on NMR shielding tensors of luciferin derivatives. *Phys Chem Liquids* **2011**, *49*, 561-571, https://doi.org/10.1080/00319101003698992.

64. Chrobak, D.; Ziółkowski, G.; Chrobak, A. On incipient plasticity of InP crystal: A molecular dynamics study. *Materials* **2021**, *14*, 4157, https://doi.org/10.3390/ma14154157.

65. Smith, J. A. S. Nuclear Quadrupole Resonance Spectroscopy. *Journal of Chemical Education.* **1971**, *48*, 39–41, https://doi.org/10.1021/ed048p39.

66. Garroway, A.N. Appendix K: Nuclear quadrupole resonance, Naval Research Laboratory. In Jacqueline MacDonald, J. R. Lockwood: *Alternatives for Landmine Detection*. Report MR-1608, Rand Corporation, **2003**. Available online: https://www.rand.org/content/dam/rand/pubs/monograph_reports/MR1608/RAND_MR1608.pdf.

67. Moudrakovski, I.L. Chapter Five - Local dynamics in hybrid perovskites by solid-state NMR. *Annual Reports on NMR Spectroscopy* **2021**, *102*, 269-341, https://doi.org/10.1016/bs.arnmr.2020.10.004.

68. Mahun,A.; Abbrent,S.; Czernek,J.; Rohlicek,J.; Macková,H.; Ning,W.; Konefał,R.; Brus,J.; Kobera,L. Reconstructing Reliable Powder Patterns from Spikelets (Q)CPMG NMR Spectra: Simplification of UWNMR Crystallography Analysis. *Molecules* **2021**, *26*, 6051, https://doi.org/10.3390/molecules26196051.

69. Monajjemi, M.; Boggs, J.E. A New Generation of BnNn Rings as a Supplement to Boron Nitride Tubes and Cages. *J. Phys. Chem. A* **2013**, *117*, 1670-1684, http://dx.doi.org/10.1021/jp312073q.

70. Monajjemi, M. Non bonded interaction between BnNn (stator) and BN B (rotor) systems: A quantum rotation in IR region. *Chemical Physics* **2013**, *425*, 29-45, https://doi.org/10.1016/j.chemphys.2013.07.014.

71. Monajjemi, M.; Robert, W.J.; Boggs, J.E. NMR contour maps as a new parameter of carboxyl's OH groups in amino acids recognition: A reason of tRNA–amino acid conjugation. *Chemical Physics* **2014**, *433*, 1-11, https://doi.org/10.1016/j.chemphys.2014.01.017.

72. Monajjemi, M. Quantum investigation of non-bonded interaction between the B15N15 ring and BH2NBH2 (radical, cation, and anion) systems: a nano molecularmotor. *Struct Chem* **2012,** *23*, 551–580, http://dx.doi.org/10.1007/s11224-011-9895-8.

73. Monajjemi, M. Metal-doped graphene layers composed with boron nitride–graphene as an insulator: a nanocapacitor. *Journal of Molecular Modeling* **2014**, *20*, 2507, https://doi.org/10.1007/s00894-014-2507-y.

74. Monajjemi, M.; Heshmat, M.; Haeri, H.H.; Kaveh, F. Theoretical study of vitamin properties from combined QM-MM methods: Comparison of chemical shifts and energy. *Russian Journal of Physical Chemistry* **2006**, *80*, 1061, https://doi.org/10.1134/S0036024406070119.

75. Fronzi, M.; Isayev, O.; Winkler, D.A.; Shapter, J.G.; Ellis, A.V.; Sherrell, P.C.; Shepelin, N.A.; Corletto, A.; Ford, M.J. Active Learning in Bayesian Neural Networks for Bandgap Predictions of Novel Van der Waals Heterostructures. *Adv. Intell. Syst.* **2021**, *3*, 2100080, https://doi.org/10.1002/aisy.202100080.

76. Fatemeh Mollaamin, Sara Shahriari, Majid Monajjemi, Zahra Khalaj, Nanocluster of Aluminum Lattice via Organic Inhibitors Coating: A Study of Freundlich Adsorption. *J Clust Sci.* **2023**, *34*, 1547−1562. https://doi.org/10.1007/s10876-022-02335-1.

77. Mollaamin, F.; Monajjemi, M. In Silico-DFT Investigation of Nanocluster Alloys of Al-(Mg,Ge,Sn) Coated by Nitrogen Heterocyclic Carbenes as Corrosion Inhibitors. *J Clust Sci.* **2023**. https://doi.org/10.1007/s10876-023-02436-5.

78. Aihara, J.; Reduced HOMO−LUMO Gap as an Index of Kinetic Stability for Polycyclic Aromatic Hydrocarbons. *J. Phys. Chem. A* **1999**, *103*, 37, 7487–7495, https://doi.org/10.1021/jp990092i.

79. Mollaamin,F.; Shahriari, S.; Monajjemi, M. DRUG DESIGN OF MEDICINAL PLANTS AS A TREATMENT OF OMICRON VARIANT (COVID-19 VARIANT B.1.1.529) .*J. Chil. Chem. Soc.* **2022**, *67* (3), 5562-5570. http://dx.doi.org/10.4067/S0717-97072022000305562.

80. Shahriari, S.; Monajjemi, M.; Mollaamin,F. DETERMINATION OF PROTEINS SPECIFICATION WITH SARS- COVID-19 BASED LIGAND DESIGNING. *J. Chil. Chem. Soc*., **2022**, *67*(2), 5468-5476. http://dx.doi.org/10.4067/S0717-97072022000205468.

81. Mollaamin,F.; Monajjemi, M. DFT outlook of solvent effect on function of nano bioorganic drugs. *Phys. Chem. Liq.* **2012**, *50* (5) , 596-604. https://doi.org/10.1080/00319104.2011.646444.

82. Mahdavian, L.; Monajjemi, M. Alcohol sensors based on SWNT as chemical sensors: Monte Carlo and Langevin dynamics simulation. *Microelectronics journal* **2010**, *41*, 142-149, https://doi.org/10.1016/j.mejo.2010.01.011.

83. Mollaamin,F.; Varmaghani, Z.; Monajjemi, M. Dielectric effect on thermodynamic properties in vinblastine by DFT/Onsager modelling. Phys. Chem. Liq. 2011, 49 (3) , 318-336 . https://doi.org/10.1080/00319100903456121.

84. Ahmadi,R.; Pishghadam, S.; Mollaamine, F.; and Zand Monfared, M.R.Comparing the Effects of Ginger and Glibenclamide on Dihydroxybenzoic Metabolites Produced in Stz-Induced Diabetic Rats.*Int J Endocrinol Metab.* **2013**,*11*, e10266. https://doi.org/10.5812/ijem.10266.